Habilitationsschrift

Faculty of Mathematics and Physics, University of Freiburg

Ab initio Simulations of Stellar Convection and Dynamos

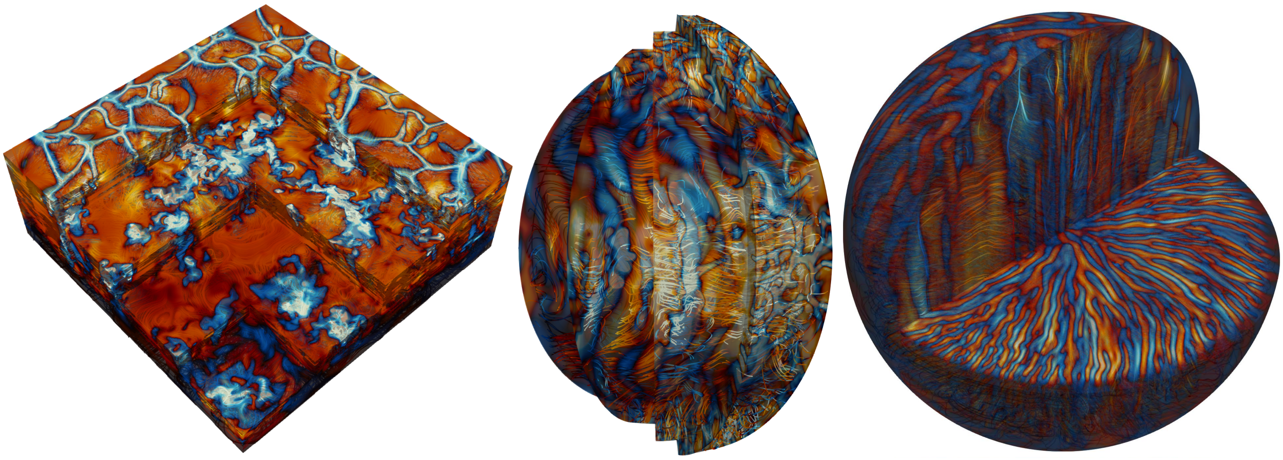

Dr. Petri J. Käpylä
Institute for Solar Physics (KIS)
Freiburg, Germany

29th March 2024

Included publications

The publications included in this dissertation are:

- **Paper I**: Käpylä, P. J., Rheinhardt, M., Brandenburg, A., Arlt, R., Käpylä, M. J., Lagg, A., Olspert, N. & Warnecke, J. 2017, "Extended subadiabatic layer in simulations of overshooting convection," *Astrophys. J. Lett.*, **845**, L23 (doi)
- **Paper II**: Viviani M., Warnecke, J., Käpylä M. J., Käpylä, P. J., Olspert, N., Cole-Kodikara, E. M., Lehtinen, J. J. & Brandenburg A. 2018, "Transition from axi- to nonaxisymmetric dynamo modes in spherical convection models of solar-like stars," *Astronomy & Astrophysics*, **616**, 160 (doi)
- **Paper III**: Käpylä, P. J. 2019, "Overshooting in simulations of compressible convection," *Astronomy & Astrophysics*, **631**, A122 (doi)
- **Paper IV**: Käpylä, P. J., Viviani, M., Käpylä, M. J., Brandenburg, A. & Spada, F. 2019, "Effects of a subadiabatic layer on convection and dynamos in spherical wedge simulations," *Geophys. Astrophys. Fluid Dyn.*, **113**, 149 (doi)
- **Paper V**: Käpylä, P. J., Gent, F. A., Olspert, N., Käpylä, M. J. & Brandenburg, A. 2020, "Sensitivity to luminosity, centrifugal force, and boundary conditions in spherical shell convection," *Geophys. Astrophys. Fluid Dyn.*, **114**, 8 (doi)
- **Paper VI**: Käpylä, P. J. 2021, "Star-in-a-box simulations of fully convective stars," *Astronomy & Astrophysics*, **651**, 66 (doi)
- **Paper VII**: Käpylä, P. J. 2021, "Prandtl number dependence of stellar convection: Flow statistics and convective energy transport," *Astronomy & Astrophysics*, **655**, 78 (doi)
- **Paper VIII**: Käpylä, P. J. 2022, "Solar-like dynamos and rotational scaling of cycles from star-in-a-box simulations," *Astrophys. J. Lett.*, **931**, L17 (doi)
- **Paper IX**: Käpylä, P. J. 2023, "Transition from anti-solar to solar-like differential rotation: Dependence on Prandtl number," *Astronomy & Astrophysics*, **669**, 98 (doi)
- **Paper X**: Käpylä, P. J. 2024, "Convective scale and subadiabatic layers in simulations of rotating compressible convection," *Astronomy & Astrophysics*, **683**, 221 (doi)

1 Introduction

Spots on the solar surface have been the source of many scientific discoveries. The first systematic observations of the Sun in the early 1600s proved the existence and variability of sunspots and dismantled the Aristotelian worldview of the perfectness and flawlessness of the Sun (e.g. Arlt & Vaquero 2020, and references therein). Longer time series of sunspot observations revealed that the Sun rotates differentially such that the rotation period at the equator is about 25 days as opposed to roughly 35 days at the poles (Carrington 1863). Now we know from helioseismology how the interior rotation rate of the Sun varies as a function of radius and latitude; see Figure 1. Furthermore, in 1843 Heinrich Schwabe postulated that the occurrence of sunspots is cyclic such that their number varies with a period of approximately 11 years (Schwabe 1844). The magnetic nature of sunspots was discovered by Hale (1908) using the Zeeman effect, and the change of the magnetic polarity from one cycle to the next by Hale *et al.* (1919). Sunspots appear at a low-latitude belt such that spots appear at mid-latitudes early in the cycle and progressively closer to the equator as the cycle advances; see Figure 2. We also know now that the cycles themselves vary on timescales of centuries and that there have been long periods when sunspots almost completely disappeared for several decades (Usoskin 2023, and references therein). The most famous of these events is the Maunder minimum which occurred soon after systematic sunspot observations commenced (Maunder 1894). The current understanding is that fluid motions inside the Sun constitute a hydromagnetic dynamo which maintains the solar magnetic field (e.g. Ossendrijver 2003; Charbonneau 2020). These motions arise because the matter in the outer parts of the Sun is very opaque and radiation becomes inefficient. The stratification is therefore convectively unstable and fluid motions transfer the heat to the surface where it is radiated into space. The interplay of these convective motions on various scales with global rotation of the Sun is thought to be the source of the differential rotation and the solar cycle (e.g. Krause & Rädler 1980; Rüdiger 1989).

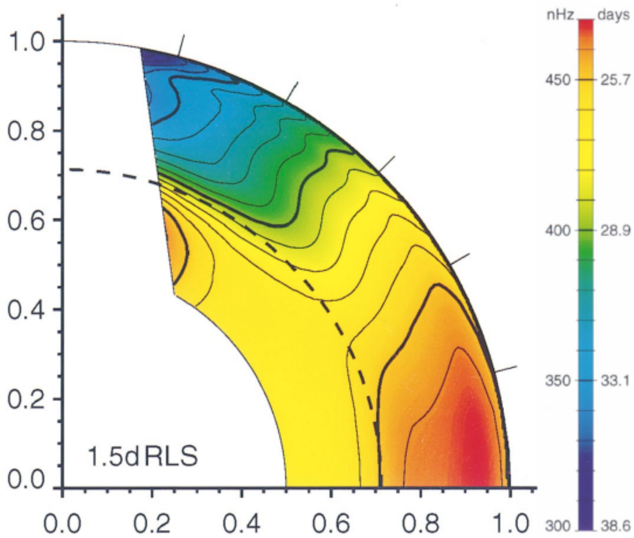

Figure 1: Solar interior rotation. Adapted from Schou *et al.* (1998).

Convection in the Sun and other stars is highly turbulent and encompasses vast ranges of temporal and spatial scales (e.g. Schumacher & Sreenivasan 2020; Jermyn *et al.* 2022). Analytic efforts to tackle the problem are thwarted because of the complexity of the flows and fields and closed-form solutions of the equations of magnetohydrodynamics (MHD) are in general practical only in rather simple cases. In a statistical approach, an equation for some suitably averaged large scales (mean or effective fields) is derived, but this equation will depend on correlations of small-scale quantities (e.g. Krause & Rädler 1980; Rüdiger 1989; Moffatt & Dormy 2019), and an infinite chain of equations emerges that constitutes the closure problem of turbulence (e.g. Speziale 1991). Despite decades of effort no generally applicable solution to this issue exists.

With the advent of the first generations of supercomputers in the 1970s and 80s, numerical solutions of the governing equations became feasible (e.g. Gilman 1977; Glatzmaier 1984). Although such simulations are still far removed from real stars, they offer a unique window into the inner workings of stellar convection zones and dynamos. Much of the initial numerical work on convection concentrated on the global aspects of large-scale flows and magnetic fields (e.g. Gilman & Miller 1981; Gilman 1983). However, after the encouraging first steps the interest in such simulations waned because their results did not match with the Sun; most importantly the magnetic fields propagated toward the poles rather than toward the equator as in the Sun. Widespread use of global simulations became mainstream much later (e.g. Brun *et al.* 2004; Ghizaru *et al.* 2010; Käpylä *et al.* 2010; Brown *et al.* 2011). Furthermore, the scope of the simulations has broadened to stars other than the current Sun ranging from solar-type stars of various ages (e.g. Ballot *et al.* 2007; Warnecke 2018; Viviani *et al.* 2018) to lower and higher mass stars with deeper (e.g. Dobler *et al.* 2006; Browning 2008; Brown *et al.* 2020) or shallower (e.g. Augustson *et al.* 2013) convection zones, and to massive stars with convective cores (e.g. Augustson *et al.* 2016).

Recent advances in helioseismology suggest that convection in the Sun is very different than in the currently used phenomenological models or in state-of-the-art 3D simulations. More specifically, the convective velocity

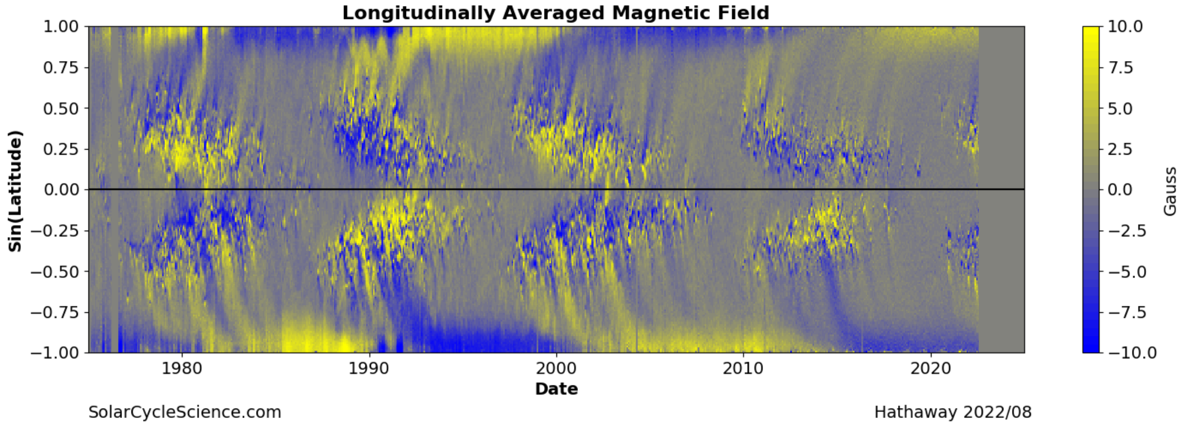

Figure 2: Longitudinally averaged solar surface magnetic field from the 1970s until the present. Courtesy of D. Hathaway, https://solarcyclescience.com.

amplitudes at large horizontal scales appear to be much smaller than anticipated from simple theoretical models or simulations (e.g. Hanasoge *et al.* 2012, 2020; Proxauf 2021). At the same time, numerical simulations are also at odds with solar observations in that models with nominally solar luminosity and rotation rate often produce anti-solar differential rotation (e.g. Käpylä *et al.* 2014). The most common interpretation of this is that the convective velocities in simulations are higher than those in the Sun, and therefore the rotational influence on convection is too weak. These discrepancies between solar observations and theoretical models are no referred to as the "convective conundrum". The cause of these differences is still under debate and this has led to a re-evaluation the fundamentals of solar and stellar convection (e.g. Brandenburg 2016). At the same time, numerical simulations remain the primary tool to study dynamo processes in stars.

The current dissertation covers numerical efforts to clarify several aspects of fundamental issues in the fields of solar and stellar convection and dynamos. The numerical approach is described in Section 2, and targeted studies of several fundamental theoretical aspects of stellar convection are presented in Section 3. Simulations targeting solar and stellar dynamos are discussed in Section 4, whereas conclusions and future prospects are summarized in Section 5.

2 Numerical simulations of stellar convection and their limitations

2.1 Relevant physics and equations

The standard way to model the flows and magnetic fields in stellar convection zones is to solve the equations of magnetohydrodynamics (MHD) in whatever geometry suits the problem at hand the best. My contributions to the field have been done with the PENCIL CODE[1] (Pencil Code Collaboration *et al.* 2021), which is a free (licensed under GNU GPL 3) finite-difference solver for ordinary and partial differential equations. The PENCIL CODE is a mature and highly flexible tool where several geometries are available for simulating convection in stars; see Figure 3 for renderings of the velocity field from Cartesian (Paper VII), spherical wedge (Paper IV), and star-in-a-box (Paper VI) models. The equations solved with the PENCIL CODE consist of the uncurled induction, continuity, Navier-Stokes, and entropy equations:

$$\frac{\partial \boldsymbol{A}}{\partial t} = \boldsymbol{u}\times\boldsymbol{B} - \eta\mu_0\boldsymbol{J}, \quad (1)$$

$$\frac{D\ln\rho}{Dt} = -\boldsymbol{\nabla}\cdot\boldsymbol{u}, \quad (2)$$

$$\frac{D\boldsymbol{u}}{Dt} = \boldsymbol{g} - \frac{1}{\rho}(\boldsymbol{\nabla}p + \boldsymbol{J}\times\boldsymbol{B} - \boldsymbol{\nabla}\cdot 2\nu\rho\mathbf{S}) - 2\boldsymbol{\Omega}\times\boldsymbol{u}, \quad (3)$$

$$T\frac{Ds}{Dt} = -\frac{1}{\rho}\left[\boldsymbol{\nabla}\cdot(\boldsymbol{\mathcal{F}}_{\rm rad} + \boldsymbol{\mathcal{F}}_{\rm SGS}) - \eta\mu_0\boldsymbol{J}^2 - \mathcal{H} + \mathcal{C}\right] + 2\nu\mathbf{S}^2, \quad (4)$$

where $\boldsymbol{A}$ is the magnetic vector potential, $\boldsymbol{u}$ is the velocity, $\boldsymbol{B} = \boldsymbol{\nabla}\times\boldsymbol{A}$ is the magnetic field, η is the magnetic diffusivity, μ_0 is the permeability of vacuum, $\boldsymbol{J} = \mu_0^{-1}\boldsymbol{\nabla}\times\boldsymbol{B}$ is the current density, ρ is the fluid density,

[1] https://pencil-code.org/

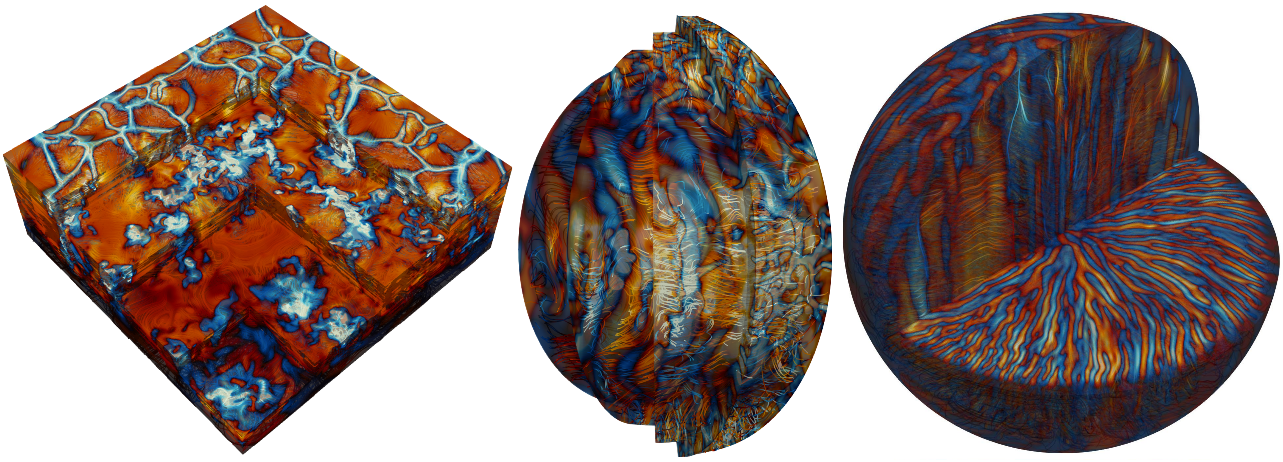

Figure 3: Examples of Cartesian (left), spherical wedge (middle), and star-in-a-box (right) convection models made with the PENCIL CODE (Pencil Code Collaboration *et al.* 2021).

$\boldsymbol{g} = -\boldsymbol{\nabla}\phi$ is the acceleration due to gravity, where ϕ is the gravitational potential, p is the gas pressure, ν is the kinematic viscosity, $\mathbf{S}$ is the traceless rate-of-strain tensor, $\boldsymbol{\Omega}$ is the rotation rate of the star, T is the temperature, s is the specific entropy, $\boldsymbol{\mathcal{F}}^{\rm rad} = -K\boldsymbol{\nabla}T$ is the radiative flux, where K is the heat conductivity, $\boldsymbol{\mathcal{F}}^{\rm SGS} = -\chi_{\rm SGS}\rho T\boldsymbol{\nabla}s'$ is the subgrid-scale (SGS) entropy flux that acts on fluctuations entropy $s' = s - \overline{s}$ from a suitably averaged profile $\overline{s}$, and $\mathcal{H}$ and $\mathcal{C}$ describe additional heating and cooling to take into account heating due to nuclear reactions in the core of the star (e.g. Dobler *et al.* 2006; Brun *et al.* 2022, see also Paper VI) and radiative losses near the surface. In all of the studies discussed in the present dissertation, the gas is assumed to be fully ionised and to obey the ideal gas equation $p = \mathcal{R}\rho T$, where $\mathcal{R} = c_{\rm P} - c_{\rm V}$ is the gas constant and $c_{\rm P}$ and $c_{\rm V}$ are the specific heat capacities in constant pressure and volume, respectively. The choice to evolve the magnetic vector potential $\boldsymbol{A}$ ensures the solenoidality of the magnetic field by construction.

2.2 System parameters and diagnostics

The simulations are described by a number of dimensionless system parameters and diagnostics. The system parameters include the thermal, SGS, and magnetic Prandtl numbers

$$\mathrm{Pr} = \frac{\nu}{\chi}, \quad \mathrm{Pr}_{\rm SGS} = \frac{\nu}{\chi_{\rm SGS}}, \quad \mathrm{Pr}_{\rm M} = \frac{\nu}{\eta}, \tag{5}$$

where $\chi = K/c_{\rm P}\rho$ is a reference value of the radiative diffusivity. Furthermore, the Taylor and Rayleigh numbers describe the effects of rotation and supercriticality of convection

$$\mathrm{Ta} = \frac{4\Omega_0^2 d^4}{\nu^2}, \quad \mathrm{Ra} = \frac{g d^4}{\nu\chi}\left(-\frac{1}{c_{\rm P}}\frac{{\rm d}s}{{\rm d}x}\right), \tag{6}$$

where $g = |\boldsymbol{g}|$, d is the depth of the convective layer, and $x \parallel -\boldsymbol{g}$. In cases with a fixed constant energy flux or luminosity, such as in all of the PENCIL CODE simulations considered here, the Rayleigh number can be expressed in terms of the energy flux $F_{\rm tot}$ as

$$\mathrm{Ra}_{\rm F} = \frac{g d^4 F_{\rm tot}}{c_{\rm P}\rho T\nu\chi^2}. \tag{7}$$

None of these parameters can be matched with the real values in the Sun and other stars in simulations: the Prandtl numbers are practically always much too large and the Rayleigh and Taylor numbers too small in simulations (see, e.g. Ossendrijver 2003; Kupka & Muthsam 2017; Käpylä *et al.* 2023). However, a number of these parameters can be combined into a modified diffusion-free flux-based Rayleigh number (Christensen 2002; Christensen & Aubert 2006)

$$\mathrm{Ra}_{\rm F}^{\star} = \frac{\mathrm{Ra}_{\rm F}}{\mathrm{Pr}^2\mathrm{Ta}^{3/2}} = \frac{g F_{\rm bot}}{8 c_{\rm P}\rho T\Omega_0^3 d^2}, \tag{8}$$

that *can* be matched in simulations; see detailed discussion in Paper X and in Section 3.2.

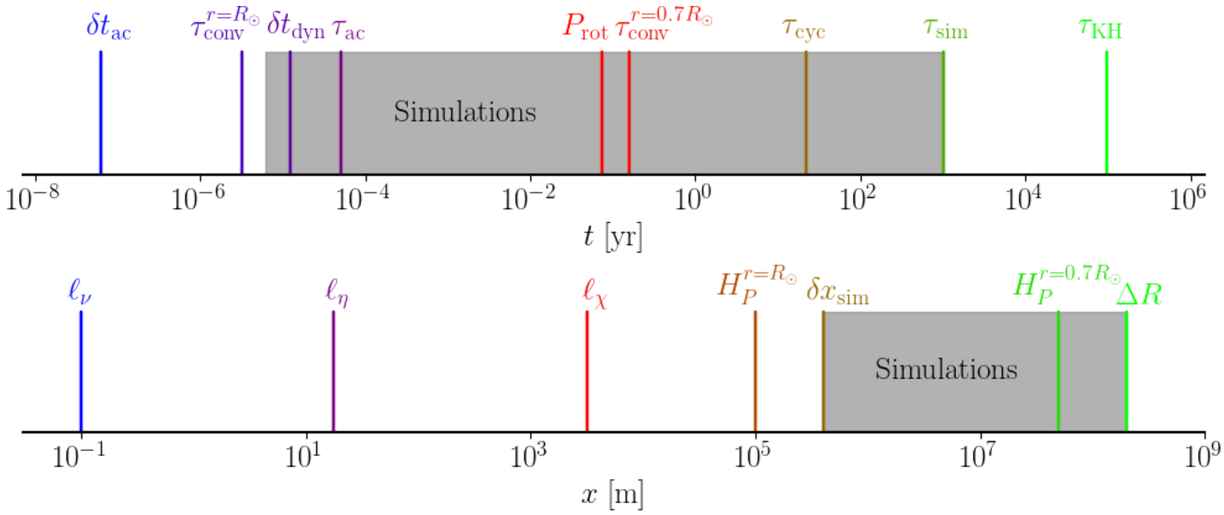

Figure 4: Timescales (top panel) and length scales (bottom panel) in the Sun. The shaded area shows the accessible range in current simulations. Adapted from Käpylä *et al.* (2023).

Diagnostics quantities include the fluid and magnetic Reynolds numbers and the thermal and SGS Péclet numbers

$$\mathrm{Re} = \frac{u_{\rm rms}}{\nu k_1}, \quad \mathrm{Re_M} = \frac{u_{\rm rms}}{\eta k_1}, \quad \mathrm{Pe} = \frac{u_{\rm rms}}{\chi k_1}, \quad \mathrm{Pe_{SGS}} = \frac{u_{\rm rms}}{\chi_{\rm SGS} k_1}, \tag{9}$$

where $k_1 = 2\pi/\Delta x$ is the wavenumber of the largest convective eddies where Δx is the depth of the convecting layer. In practically all simulations $\mathrm{Pr_{SGS}} \gg \mathrm{Pr}$ and therefore $\mathrm{Pe} \gg \mathrm{Pe_{SGS}}$, meaning that the SGS entropy diffusion is dominant in smoothing small-scale entropy fluctuations (see Appendix A of Käpylä *et al.* 2017). The Reynolds and Péclet numbers are again much larger in real stars than in any current simulation (see, e.g. Käpylä *et al.* 2023). The influence of rotation on the flow is characterized by the global and local Coriolis numbers

$$\mathrm{Co} = \frac{2\Omega_0}{u_{\rm rms} k_1}, \quad \mathrm{Co}_\ell = \frac{2\Omega_0 \ell}{u_{\rm rms}}, \tag{10}$$

which is the only diagnostics that can be captured by simulations. The former definition does not take into account the changing scale of convection, whereas the in the latter the length scale ℓ is also a result of the simulation; see, e.g., Aurnou *et al.* (2020) and Paper X.

2.3 Simulation strategy: Enhanced luminosity method (Paper III and Paper V)

Simulations of stellar convection and dynamos face a terrific numerical challenge because of the vast variety of spatial and temporal scales in stellar convection zones (see Käpylä *et al.* 2023, for a recent review). Figure 4 summarizes the ranges of these scales in the Sun and the range currently accessible for global simulations. A primary challenge is that in the general fully compressible case the timestep in the simulations is determined by the speed of sound in the deep interior which is by far the fastest signal propagation speed. The acoustic timestep is $\delta t_{\rm ac} \propto \delta x/c_{\rm s}$, where δx is the grid spacing in the simulation and $c_{\rm s}$ the sound speed. In a simulation of the full Sun this leads to a timestep that is a fraction of a second with currently typical grid resolution of around 500^3 grid points (Käpylä *et al.* 2023). The timestep issue is typically alleviated by the use of the anelastic approximation (e.g. Lantz & Fan 1999) where sound waves are filtered out and the timestep is determined by the dynamical timestep $\delta t_{\rm dyn} \propto \delta x/u$ which is two to three orders of magnitude larger than $\delta t_{\rm ac}$ in the deep convection zone. At the other end of the spectrum is the thermal relaxation or Kelvin-Helmholtz time $\tau_{\rm KH} = GM^2/2RL$, where G is the gravitational constant and M, R, and L are the mass, radius, and luminosity of the star. For the whole Sun $\tau_{\rm KH} \approx 2\cdot 10^7$ years. This is much longer than the affordable integration times for numerical simulations which are typically run for tens to hundreds of years in physical time, with the longest simulations being of the order of $\tau_{\rm sim} \approx 10^3$ years (e.g. Passos & Charbonneau 2014). Typical anelastic simulations assume the real stellar luminosity which means that covering $\tau_{\rm KH}$ in such models is infeasible and thermal relaxation is not necessarily guaranteed. There is also a computational penalty for using the anelastic method: a global solution of a Poisson equation is required at every timestep which becomes a limiting factor

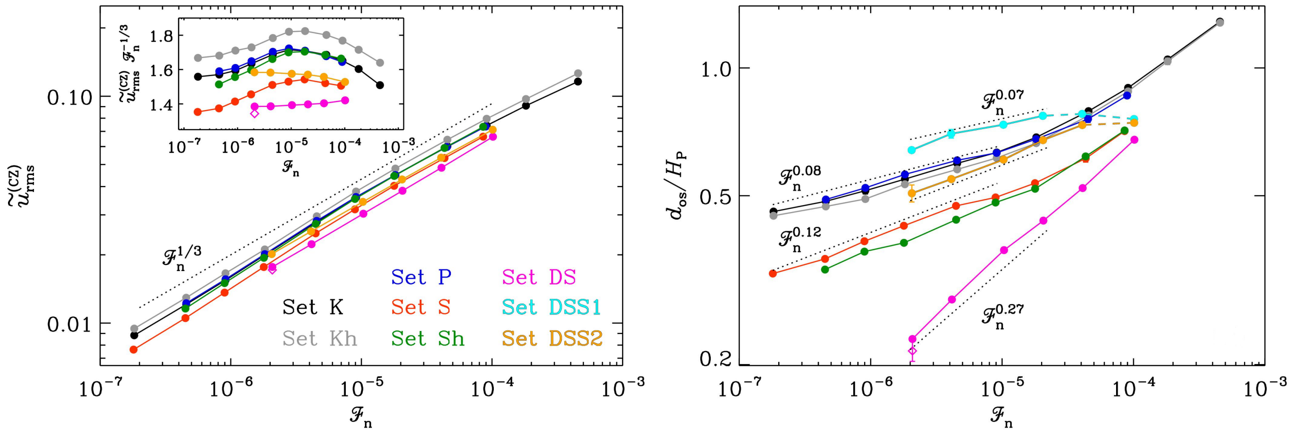

Figure 5: Left panel: rms velocity averaged over the convection zone as a function of normalized flux $\mathscr{F}_{\rm n}$. Right panel: overshooting depth $d_{\rm os}$ normalized by the pressure scale height H_P at the base of the convection zone as a function of $\mathscr{F}_{\rm n}$ from the same simulations. Adapted from Paper III.

for the scaling of such codes to very high numbers of CPUs or GPUs. Further relevant timescales that the simulations also need to resolve include the acoustic (free-fall) time $\tau_{\rm ac} = \sqrt{GM/R^3}$, convective turnover time $\tau_{\rm conv} = \ell/u_{\rm conv}$ where $u_{\rm conv}$ is the convective velocity, and the magnetic cycle period $\tau_{\rm cyc}$ which is 22 years for the Sun.

The PENCIL CODE simulations approach the timescale issue from a different angle and solve the fully compressible equations where the full time dependence of density is retained. Instead of eliminating the sound waves, the simulations use a higher luminosity ($\mathcal{L}_{\rm sim}$) than in real stars ($\mathcal{L}_\star$) which is referred to the enhanced luminosity method (ELM). This brings the dynamical and acoustic timescales closer to each other by increasing the Mach number, ${\rm Ma} = u_{\rm rms}/c_{\rm s}$, of the flows. Typical luminosity enhancement ratio $L_{\rm ratio} = \mathcal{L}_{\rm sim}/\mathcal{L}_\star$ in simulations targeting the Sun is of the order of 10^6 (e.g. Käpylä *et al.* 2014). Assuming a balance between advective and buoyancy forces and that convection transports all of the energy leads to a scaling $u_{\rm conv} \propto L_{\rm ratio}^{1/3}$; see, e.g., Appendix A of Paper X. Therefore the convective velocity is enhanced by a factor of 10^2 in the aforementioned simulation targeting the Sun. Nevertheless, in such simulations ${\rm Ma} \approx 10^{-2} \ldots 0.1$ which means that the flows are still clearly subsonic. Furthermore, $\tau_{\rm KH} \propto L_{\rm ratio}^{-1}$, meaning that the Kelvin-Helmholtz timescale can be resolved in such simulations (see, Paper IX). Another advantage is that no global Poisson problem has to be solved and the numerical algorithm can be based on local stencils.

The scaling of convective rms velocity as a function of the normalized flux $\mathscr{F}_{\rm n}(\propto \mathcal{L}_{\rm sim})$ was studied in Paper III from non-rotating hydrodynamic simulations; see the left panel of Figure 5. The scaling holds at least in the range of parameters that are accessible to simulations currently. The enhanced velocities necessitate that also the rotation rate Ω has to be increased with the same factor to capture the same rotational influence on the flows as in the target star. The detailed scaling relations between simulations using ELM and physical units were derived in Appendix A of Paper V. The tradeoff in ELM is that it is no longer the target star that is modeled but rather an analogue with enhanced luminosity. The higher velocities in such simulations are anticipated to lead to more mixing in the boundary layers between convectively stable and unstable layers. Earlier numerical studies have reported steep, roughly $\mathscr{F}_{\rm n}^{1/3}$ dependence of the overshooting depth (e.g. Singh *et al.* 1998; Tian *et al.* 2009; Hotta 2017). The main result of Paper III is that eliminating dependencies on other quantities such as the Reynolds and in particular the Prandtl number, a much shallower dependence with $\mathscr{F}_{\rm n}^{0.08}$ was found; see the right panel of Figure 5. This implies that in a simulation with $L_{\rm ratio} = 10^6$, convective overshooting is only about three times deeper than in the actual star. This is a relatively mild tradeoff to balance with the benefits of bringing the timescales substantially closer to each other. In Paper V it was shown that the differential rotation and large-scale thermodynamic structures, such as the thermal wind balance achieved in semi-global simulation,s were essentially unchanged when the Mach number was varied by changing $L_{\rm ratio}$.

The issues with length scales seem at first glance even more severe than those of the timescales; see the lower panel of Figure 4. The scales at which molecular diffusion takes over are many orders of magnitude lower than the grid scale $\delta x_{\rm sim}$ in even the highest resolution simulations to date (Käpylä *et al.* 2023). For example, the Kolmogorov scale ℓ_ν where kinetic energy thermalizes in the solar convection zone is of the order of 10 cm (e.g. Kupka & Muthsam 2017; Schumacher & Sreenivasan 2020). The ratio $\Delta R/\ell_\nu \approx 2 \cdot 10^9$, where ΔR is the depth of the convection zone, gives an estimate of the number of grid points per direction in a direct numerical simulation (DNS) of the solar convection zone. The largest global simulations to date have a few thousand grid points per direction (e.g. Hotta *et al.* 2022). It is highly unlikely that a DNS of the Sun would be possible with semiconductor-based CPUs and GPUs (see the discussions in Kupka & Muthsam 2017; Käpylä *et al.* 2023). Furthermore, the Kolmogorov scale is much smaller than the corresponding scales for magnetic fields (ℓ_η) or temperature (ℓ_χ), such that $\ell_\nu \ll \ell_\eta \ll \ell_\chi$, so that the corresponding Prandtl numbers $\mathrm{Pr}, \mathrm{Pr_M} \ll 1$ (e.g. Schumacher & Sreenivasan 2020). While the timescale issue can be to a certain degree circumvented, no similar remedy is available for the spatial scales. However, it is plausible that the large-scale phenomena such as differential rotation and global magnetic fields can be captured at a much lower resolution than that of a DNS when sufficiently many scales are included. It is not yet clear if such asymptotic regime has been reached in simulations (e.g. Käpylä *et al.* 2017; Hotta *et al.* 2022; Guerrero *et al.* 2022).

3 The changing paradigm of stellar convection

The helioseismic inferences regarding the lower than expected velocity amplitudes at large horizontal scales in the Sun are at odds with the standard models of stellar convection. In the most commonly used theoretical descripton used in 1D stellar structure models, the mixing length theory (e.g. Vitense 1953; Böhm-Vitense 1958), the gas is considered to consists of discrete convective elements or blobs, whose size is proportional to the local pressure scale height H_p. These convective elements are assumed to dissolve to the surrounding medium after traveling a mixing length $\ell_\mathrm{mix} = \alpha H_\mathrm{p}$, where α is a tunable parameter of the order of unity. The theory further assumes that convection is driven locally by an unstable entropy gradient according to the Schwarzschild criterion

$$\nabla - \nabla_\mathrm{ad} = -\frac{H_\mathrm{p}}{c_\mathrm{P}}\frac{\mathrm{d}s}{\mathrm{d}x} > 0, \tag{11}$$

where $\nabla = \partial \ln T/\partial \ln p$ is the logarithmic temperature gradient, and $\nabla_\mathrm{ad} = 1 - 1/\gamma$ is the corresponding adiabatic gradient. Following these assumptions to their logical consequences implies that the size of convection cells increases with depth and that the largest convectively driven scale coincides with the depth of the convective layer. For the Sun this corresponds to a scale of the order of 200 Mm which is referred to as giant cell convection.

This is in contrast to the dominant scale of convection in the Sun which appears to be much smaller ($20\ldots30$ Mm), and coincides with that of supergranulation (e.g. Proxauf 2021); see, however, Greer *et al.* (2015). Giant cells appear to be extremely weak in the Sun while they are very prominent in numerical simulations of global convection (e.g. Miesch *et al.* 2008). Therefore premise of convection being driven locally by an unstable entropy gradient everywhere in the convection zone has been questioned (e.g. Brandenburg 2016). Furthermore, the mixing length theory does not take into account rotation or magnetic fields which have also been invoked to explain the differences between observations and models (e.g. Featherstone & Hindman 2016; Hotta *et al.* 2022). Finally, the system parameters of simulations, such as the Prandtl number, are often chosen for their numerical convenience rather than physical accuracy. In my work I have studied each of these possibilities with targeted simulations. These results will be reviewed in the following sections.

3.1 Non-local surface driving of convection (Paper I)

Early simulations of solar surface convection suggested that convection is highly non-local and driven by the cooling at the surface rather than the local entropy gradient (Stein & Nordlund 1989, 1998). These ideas were further elaborated by Spruit (1997) who envisioned plumes or filaments that traverse the whole depth of the convection zone. Such cool *entropy rain* was implemented in an extended mixing length model by Brandenburg (2016), who showed that under certain conditions most of the convection zone can be weakly stably stratified. Numerical simulations of stellar convection have to a large extent adapted the mixing length philosophy in that a superadiabatic temperature gradient appears throughout the convection zone. Typically this is done by enforcing a fixed heat conductivity profile $K = K(\boldsymbol{x})$ which is independent of the ambient thermodynamics (see discussion in Paper I). In reality K is given by

$$K = \frac{16\sigma_\mathrm{SB}T^3}{3\kappa\rho}, \tag{12}$$

where σ_SB is the Stefan–Boltzmann constant and κ is the opacity.

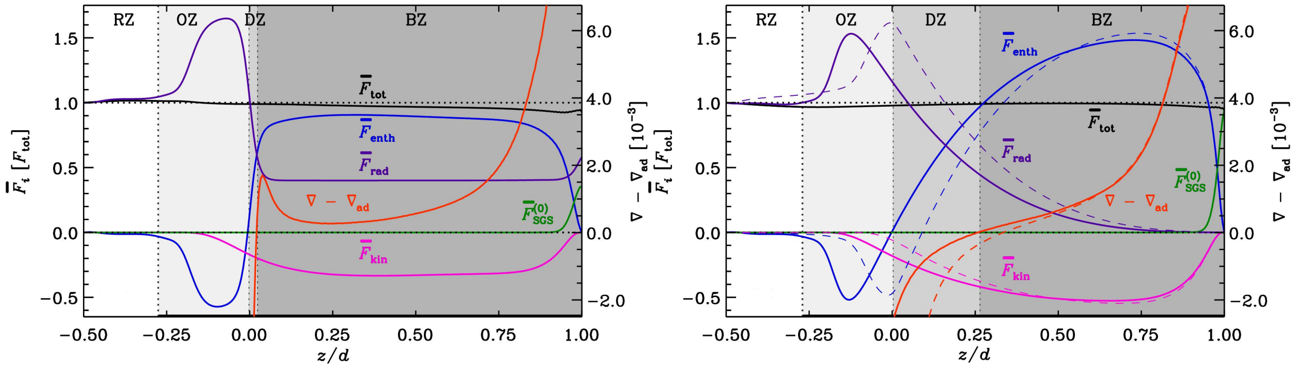

Figure 6: Left panel: Horizontally averaged energy fluxes from a simulation with a spatially fixed step profile for K. $\overline{F}^{(0)}_{\rm SGS}$ is an SGS flux that acts on the mean entropy gradient (see discussion in Paper I), and the red curve denotes the superadiabatic temperature gradient $\nabla - \nabla_{\rm ad}$. Right panel: similar simulation but with Kramers opacity law (solid lines) and a run with similar spatially fixed but smoothly varying K (dashed). Adapted from Paper I.

In Paper I the assumption of spatially fixed K was relaxed in simulations of convection in Cartesian geometry, and a power law was assumed for the opacity

$$\kappa = \kappa_0 \left(\frac{\rho}{\rho_0}\right)^a \left(\frac{T}{T_0}\right)^b, \quad \text{which leads to} \quad K = K_0 \left(\frac{\rho}{\rho_0}\right)^{-(a+1)} \left(\frac{T}{T_0}\right)^{3-b}, \tag{13}$$

where ρ_0 and T_0 are reference values for density and temperature, and where K_0 subsumes the constants κ_0 and $\sigma_{\rm SB}$. The choice $a = 1$, $b = 7/2$ corresponds to Kramers opacity law which approximates the opacity in, for example, the solar convection zone (e.g. Weiss *et al.* 2004). The advantage of the Kramers opacity is that because of its analytic form, it is very easy to implement in a numerical model. Although some early studies used Kramers conductivity in simulations (Edwards 1990; Brandenburg *et al.* 2000), its use is still not widespread. The novelty of the Kramers opacity lies in that changes in the ambient thermodynamic state are immediately taken into account and the effects of additional physics such as magnetism and rotation are thus indirectly imprinted in the heat conductivity. Furthermore, the heat conductivity profile connects radiative and convective layers smoothly allowing a more natural boundary between these zones.

In simulations with a step profile of heat conductivity, the convection zone depth is fixed from the outset; see the left panel of Figure 6. In such setups the convective enthalpy flux $\overline{F}_{\rm enth} = c_{\rm P}\overline{(\rho u_z)'T'}$ is outward only if $\nabla - \nabla_{\rm ad} > 0$. We can identify the buoyancy zone (BZ) where $\overline{F}_{\rm enth} > 0$ and $\nabla - \nabla_{\rm ad} > 0$, an overshoot zone (OZ) where $\overline{F}_{\rm enth} < 0$ and $\nabla - \nabla_{\rm ad} < 0$, and a radiative zone (RZ) where $\overline{F}_{\rm enth} \approx 0$ and $\nabla - \nabla_{\rm ad} < 0$. On the other hand, in cases where the radiative and convective regions connect smoothly, such as with the Kramers opacity or a similar fixed but smoothly varying profile, the lower convection zone is formally stably stratified; see the right panel of Figure 6. Therefore a new layer, the Deardorff zone (DZ), appears which is absent in canonical models of convection, and where $\overline{F}_{\rm enth} > 0$ and $\nabla - \nabla_{\rm ad} < 0$. These results suggest that the deep parts of the solar convection zone can be stably stratified. However, the Deardorff zone in these and other similar simulations (e.g. Tremblay *et al.* 2015; Hotta 2017) is still a relatively shallow compared to the total depth of the convectively mixed layer, and the power spectrum of convective velocity still peaks at the largest horizontal scales (see, e.g., Paper VII).

Although insufficient to solve the convective conundrum, these results have repercussions in mean-field theory of hydrodynamics. The Schwarzschild criterion is often imprinted here as well, such that the suitably averaged net convective enthalpy flux is parameterized by a gradient diffusion term (e.g. Rüdiger 1989)

$$\overline{\boldsymbol{F}}^{\rm (MF)}_{\rm enth} = -\chi_{\rm t}\overline{\rho}\overline{T}\boldsymbol{\nabla}\overline{s} \equiv \boldsymbol{F}_G, \tag{14}$$

where $\chi_{\rm t}$ is a turbulent thermal diffusivity. The importance of non-local effects was realized in the atmospheric physics community already in the 1960s where a corresponding non-gradient term was included in the expression of the enthalpy flux (Deardorff 1961, 1966) with

$$\overline{\boldsymbol{F}}^{\rm (MF)}_{\rm enth} = -\chi_{\rm t}\overline{\rho}\overline{T}\boldsymbol{\nabla}\overline{s} + \tau_{\rm rel}\overline{\rho}\overline{T}\,\overline{s'^2}\boldsymbol{g}/c_{\rm P} \equiv \boldsymbol{F}_G + \boldsymbol{F}_D, \tag{15}$$

where $\tau_{\rm rel}$ is a relaxation time, and where the latter *Deardorff flux* $\boldsymbol{F}_D$ is positive irrespective of the sign of the entropy gradient. In stars such as the Sun the latter term is thought to arise because convection is driven by the cooling at the surface leading to highly non-local downflow plumes that can penetrate the entire convection zone. This is illustrated in Figure 7 which shows the total force $\overline{f}_z = \overline{\rho D u_z/Dt}$ on upflows and downflows for a simulation similar to that in the right panel of Figure 6. The downflows are accelerated downward near the surface where $\overline{f}_z < 0$, and they are decelerated in the Schwarzschild stable Deardorff (DZ) and overshoot zones (OZ). The apparent adherence of the forces on the downflows to the Schwarzschild criterion is partly a coincidence and in other similar simulations this is less apparent (see, e.g., Fig. 21 of Paper VII and Fig. 12 of Paper X). On the other hand, the upflows are accelerated upward everywhere except near the surface. Such upward acceleration cannot be because of the convective instability in the stably stratified OZ and DZ regions. It is rather the result of the deeply penetrating downflows that displace the matter in the deep parts and drive upflows by pressure forces. The fact that also the upflows appear to be driven by a secondary effect of surface-originating plumes is a clean break from the canonical picture of convection where the driving is done everywhere locally by a negative entropy gradient.

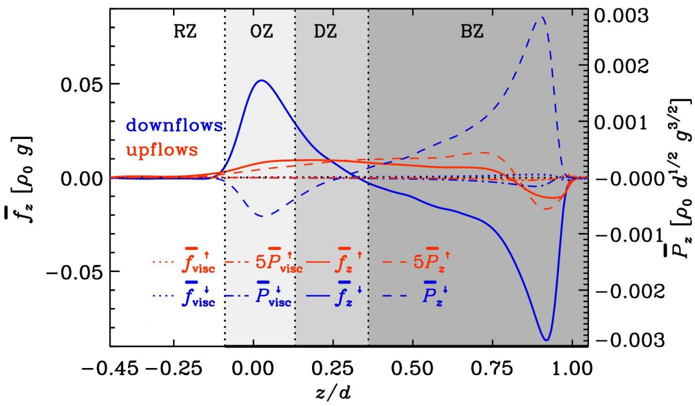

Figure 7: Horizontally averaged forces ($\overline{f}_z$) on upflows (red) and downflows (blue) from a Kramers convection simulation. The dashed lines show the corresponding power. Adapted from Paper III.

3.2 Rotational constraint in the deep solar convection zone (Paper X)

As mentioned above, mixing length theory does not take into account dynamical effects such as rotation or magnetic fields. In Paper X the effects of rotation on convection were probed with hydrodynamic 3D simulations in Cartesian geometry. Rotation has a significant impact on the excitation conditions of convection in the linear regime (e.g. Chandrasekhar 1961; Roberts 1968). This includes a shift of the most unstable mode to higher wavenumbers or smaller spatial scales. Such effects are expected to be carried over to nonlinear dynamics of convection if the Coriolis number

$$\mathrm{Co} = \frac{2\Omega_0}{u_{\rm conv} k_1}, \tag{16}$$

is sufficiently large. This is encapsulated in a generalized rotating mixing length theory (e.g. Stevenson 1979; Barker *et al.* 2014; Aurnou *et al.* 2020), where a balance between Coriolis, inertial, and buoyancy (Archimedean) forces is assumed (CIA balance). This theory predicts that the dominant length scale of convection scales as

$$\ell \propto \mathrm{Co}^{-1/2}, \tag{17}$$

for $\mathrm{Co} \gtrsim 1$ (e.g. Vasil *et al.* 2021, Paper X). Using the velocity and length scales from mixing length theory, Co is expected to exceed unity around $r = 0.95 R_\odot$ and reach values of the order of ten near the base of the solar convection zone (e.g. Käpylä *et al.* 2005; Schumacher & Sreenivasan 2020). Therefore the dominant convective scale should be affected in much of the solar convection zone.

This idea was picked up by Featherstone & Hindman (2016) and Vasil *et al.* (2021), who argued that deep convection in the Sun is sufficiently strongly rotationally constrained that the dominant convective scale coincides with the scale of supergranulation. Using global 3D numerical simulations of rotating convection, Featherstone & Hindman (2016) showed that such situation is obtained when $\mathrm{Co} \approx 17$ (see detailed discussion in Paper X). There is currently no observational technique to ascertain this and therefore we do not have empirical data for ℓ or u in the deep solar convection zone. It is furthermore unclear whether the simulation parameters of Featherstone & Hindman (2016) correspond to the Sun. This was clarified in Paper X, where a new Coriolis number independent of any dynamical length scale or velocity was introduced. This quantity turns out to be a system parameter that must be matched with the target star, e.g., the Sun in this case. We call this the *flux Coriolis number*, and it is given by

$$\mathrm{Co_F} = 2\Omega H \left(\frac{\rho_\star}{F_{\rm tot}}\right)^{1/3}, \tag{18}$$

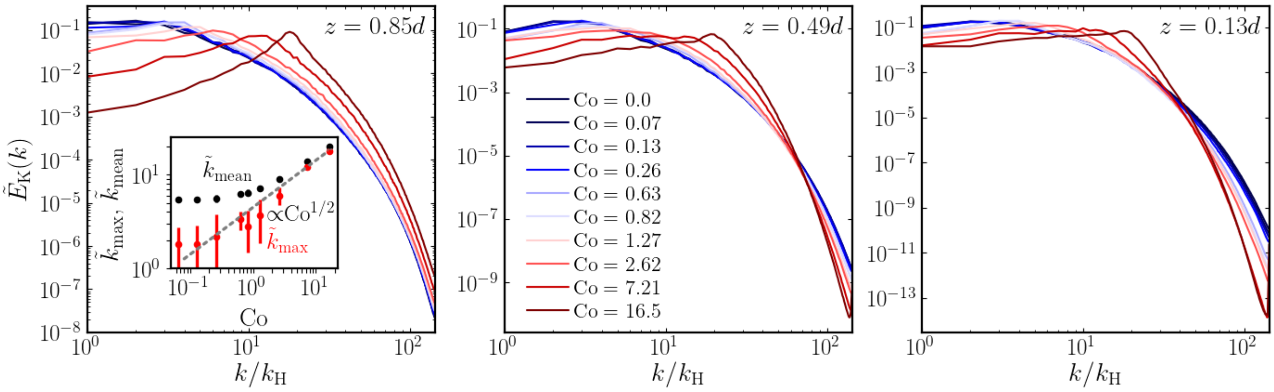

Figure 8: Normalized power spectra of velocity $\tilde{E}_K(k) = E_K(k)/\int E_K(k)dk$ at three depths within the convection zone for a set of runs where Co varies between 0 and 16.5. The inset in the left panel shows the mean ($\tilde{k}_{mean} = k_{mean}/k_H$) and maximum ($\tilde{k}_{max} = k_{max}/k_H$) wavenumbers as functions of Co for $z/d = 0.85$. The grey dashed line shows a power law proportional to $Co^{1/2}$. Adapted from Paper X.

where H is a length scale, $\rho_\star$ is a reference density, and F_{tot} is the total energy flux emanating from the radiative core. Furthermore, with a suitable choice of the length scale H, Co_F can be written as

$$Co_F = (Ra_F^\star)^{-1/3}, \text{ where } Ra_F^\star = \frac{F_{bot}}{8\rho_\star\Omega^3H^3}, \tag{19}$$

is the modified diffusion-free flux-based Rayleigh number (Christensen 2002; Christensen & Aubert 2006). Choosing $H = H_p$, where H_p is the pressure scale height at the base of the convection zone, all of the quantities in Eq. (18) are known from either from direct observations (F_{bot}, Ω) or from solar interior models ($\rho_\star$, H_p). Therefore it is possible to construct simulations where the forcings due to luminosity and rotation match precisely those of the Sun.

Before discussing the solar case in detail, the overall results from Paper X regarding rotational scaling are shown in Figs. 8 and 9. The convective scale is estimated from the power spectrum of the velocity field $E_K(k)$ for which $\boldsymbol{u}^2 = \int E_K(k)dk$. The convective scale was determined either by considering the wavenumber $k = k_{max}$ where the E_K has its maximum, or by taking the mean wavenumber $k_{mean} = \int kE_K(k)dk/\int E_K(k)dk$. Figure 8 shows that for slow rotation ($Co \lesssim 1$) the convective scale is almost unaffected by rotation, whereas for sufficiently rapid rotation ($Co \gtrsim 3$) the scaling proportional to $Co^{1/2}$ is obtained in accordance with the CIA balance. Similarly the relation between Co_ℓ and Co is linear until around $Co = 1$ and approaches $Co_\ell \propto Co^{1/2}$ for the most rapidly rotating cases; see Figure 9. Furthermore, the scaling of Co_ℓ as a function of $Ra_F^\star$ changes from $(Ra_F^\star)^{-1/3}$ for slow rotation to $(Ra_F^\star)^{-1/5}$ for rapid rotation. All of these results are in accordance with the scalings derived under the CIA balance (Stevenson 1979; Barker *et al.* 2014; Aurnou *et al.* 2020, Paper X).

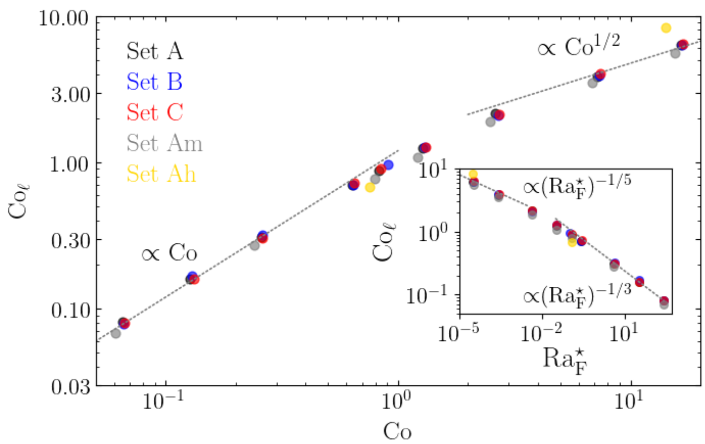

Figure 9: Co_ℓ as a function of Co along with theoretical scalings for slow and rapid rotation. The inset shows Co_ℓ as a function of $Ra_F^\star$ with corresponding theoretical scalings. Adapted from Paper X.

In Paper X it was shown that in the Sun the flux Coriolis number is $Co_F^\odot \approx 3.14$ using values of the density and pressure scale height from the base of the convection zone. The relation between Co and Co_F is given by

$$Co = \frac{u_\star}{u}\frac{Co_F}{k_1 H_p}, \tag{20}$$

where $u_\star = (F_{bot}/\rho_\star)^{1/3}$ is a reference velocity that measures the available flux. For the simulations in Paper X, $Co \approx 0.87$ for $Co_F^\odot$. Inspection of Figure 8 reveals that the convective scale is almost unchanged from the non-rotating case for this Coriolis number. A more detailed calculation involving a scaling back to physical units gives estimates $\ell_{\max} \approx 135$ Mm and $\ell_{\rm mean} \approx 58$ Mm from the maximum and mean wavenumbers, respectively. Both estimates clearly exceed the supergranular scale of $20\ldots30$ Mm in the Sun. Furthermore, the simulations of Featherstone & Hindman (2016) that yielded the $\ell_{\max} \approx 25$ Mm with Co ≈ 17 were shown to have a rotation rate corresponding to at least $15\Omega_\odot$. These results suggest that rotationally constrained convection cannot explain the low velocity amplitudes at large scales in the Sun.

3.3 Effect of Prandtl number

As discussed in Section 2.2, current or any foreseeable numerical simulations are unable to reach realistic parameter regimes relevant for stellar interiors. This raises questions regarding the applicability of the simulation results to astrophysical conditions. One such issue is that in the Sun and in most stellar convection zones the thermal Prandtl number is $\mathrm{Pr} \ll 1$ (e.g Augustson *et al.* 2019; Jermyn *et al.* 2022), whereas numerical simulations are restricted to values close to $\mathrm{Pr} = 1$. A concrete effect of this was discovered in Paper III where overshooting below the convection zone was found to be sensitive to the Prandtl number. More specifically, the steep dependence of overshooting depth as a function of luminosity found in earlier studies was shown to be explained largely by the variation of the Prandtl number; see Section 2.3. Prandtl number dependence has also been suggested as a solution to the convective conundrum. However, this has been approached from the perspective that the effective (turbulent) Prandtl number in the Sun is greater than unity. Numerical simulations indeed suggest that increasing the Prandtl number leads to a reduction of the overall velocity amplitudes (O'Mara *et al.* 2016; Bekki *et al.* 2017; Karak *et al.* 2018; Orvedahl *et al.* 2018), but there is also evidence that it becomes harder to maintain a solar-like rotation profile in such simulations despite the lower velocities (Karak *et al.* 2018). Finally, earlier analytic (Spiegel 1962) and numerical (e.g. Cattaneo *et al.* 1991; Breuer *et al.* 2004; Pandey *et al.* 2021) work has shown that convection in the regime $\mathrm{Pr} \ll 1$ is qualitatively different from the $\mathrm{Pr} = 1$ case. More specifically, convection becomes highly inertial and coherent large-scale structures are intensified, along with a redistribution of the convective flux between the upflows and downflows. These considerations led to two studies where I studied the energy transport and flow structure in Cartesian geometry (Paper VII) and the effects Prandtl number on differential rotation in semi-global simulations (Paper IX).

3.3.1 Convective energy transport and flow structure (Paper VII)

The dependence of convective energy transport on the Prandtl number is illustrated in the left panel of Figure 10, where the convected flux (Cattaneo *et al.* 1991) according to

$$\overline{F}_{\rm conv} = \overline{F}_{\rm enth} + \overline{F}_{\rm kin}, \tag{21}$$

where $\overline{F}_{\rm kin} = \frac{1}{2}\overline{\rho \boldsymbol{u}^2 u_z}$ is the kinetic energy flux, along with $\overline{F}_{\rm enth}$ and $\overline{F}_{\rm kin}$ are shown from simulations $\mathrm{Pr}_{\rm SGS}$ ranging between 0.1 and 10 (Paper VII). The simulation setup was chosen such that the SGS diffusivity is dominant in smoothing the small-scale entropy fluctuations, i.e., $\mathrm{Pr} \gg \mathrm{Pr}_{\rm SGS}$. Furthermore, the SGS diffusivity acts only on the fluctuations of entropy and does not therefore directly contribute to the net energy transport. This means that the driving of convection, either by surface cooling or an unstable entropy gradient is nearly unaffected when $\mathrm{Pr}_{\rm SGS}$ is varied. This is manifested by the practically identical $\overline{F}_{\rm conv}$ within the convection zone as a function of $\mathrm{Pr}_{\rm SGS}$. However, the mean enthalpy and kinetic energy fluxes are sensitive to the Prandtl number: the absolute magnitudes of both $\overline{F}_{\rm enth}$ and $\overline{F}_{\rm kin}$ increase with decreasing $\mathrm{Pr}_{\rm SGS}$. Because they have opposite signs, a larger convective velocities are needed to transport the same flux for lower $\mathrm{Pr}_{\rm SGS}$.

A striking effect of the changing convective velocities is that overshooting below the convection zone is highly sensitive to the Prandtl number. The region of overshoot with $\overline{F}_{\rm conv} < 0$ below about $z/d = 0.1$ becomes progressively deeper with decreasing $\mathrm{Pr}_{\rm SGS}$. This is shown in more detail in the right panel of Figure 10 which shows the overshooting depth $d_{\rm os}$ measured from the kinetic energy flux as a function of $\mathrm{Pr}_{\rm eff}$[2] and Pe (see Paper VII for detailed definition of overshooting the depth). There is a monotonic increase of $d_{\rm os}$ with decreasing $\mathrm{Pr}_{\rm eff}$, although when the Péclet number is increased this trend is somewhat weaker. This nevertheless raises the question of the nature of convective overshooting in, for example, in the Sun where $\mathrm{Pr} \approx 10^{-6}$ in comparison to current numerical work with $\mathrm{Pr} \approx 1$.

Another important finding in Paper VII is related to the filling factor f of downflows. The relevance of f is that it traces the asymmetry between upflows and downflows which is the principal reason for the

[2] $\mathrm{Pr}_{\rm eff} = \nu/(\chi + \chi_{\rm SGS})$, where χ is a reference value from $z/d = 0.85$. In practice $\mathrm{Pr}_{\rm eff} \approx \mathrm{Pr}_{\rm SGS}$ in the bulk of the convection zone, see Table 1 of Paper VII.

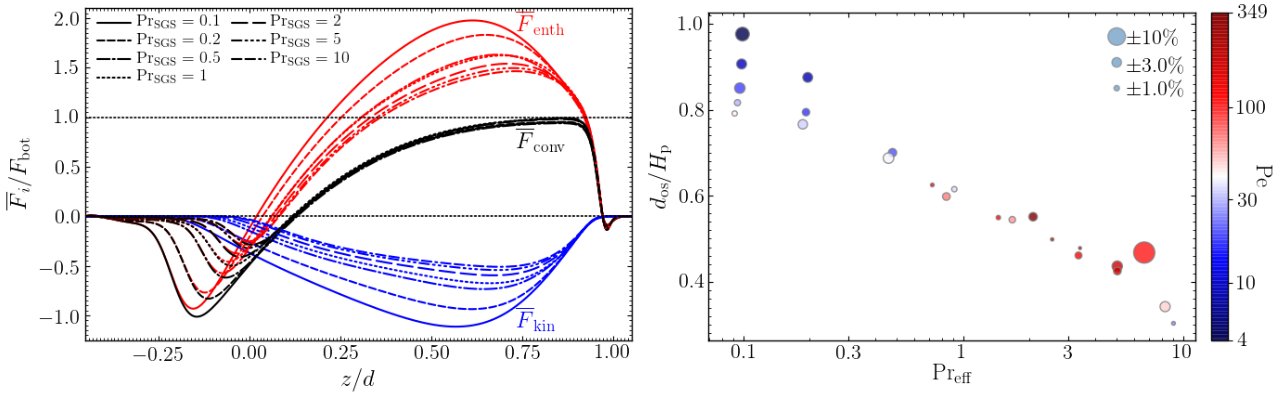

Figure 10: Left panel: Horizontally averaged convected flux according to Eq. (21), along with convective enthalpy ($\overline{F}_{\rm enth}$) and kinetic energy fluxes ($\overline{F}_{\rm kin}$), as functions of the SGS Prandtl number. Right panel: Overshooting depth $d_{\rm os}$ as a function of the effective Prandtl number $\mathrm{Pr_{eff}}$. Adapted from Paper VII.

appearance of the Deardorff zone (see detailed discussion in Paper X). Furthermore, a very small filling factor (as low as 10^{-4}) is typically assumed in semi-analytic models of convection that produce Deardorff layers; see, for example, Rempel (2004) and Brandenburg (2016). The results of Paper VII indicate that the filling factor is sensitive to $\mathrm{Pr_{SGS}}$ such that f decreases with $\mathrm{Pr_{SGS}}$; see Figure 11. This can be interpreted such that fewer but stronger downflows are present when the Prandtl number decreases. However, even the lowest local values obtained in these simulations are of the order of 0.25 which is several orders of magnitude larger than the values adopted in the semi-analytic models mentioned above. On the other hand, the Prandtl number is still five orders of magnitude larger in the simulations than in the deep convection zone of the Sun. Therefore the results of Paper VII hint at the intriguing possibility that convection in the Sun is qualitatively different from what the current simulations suggests.

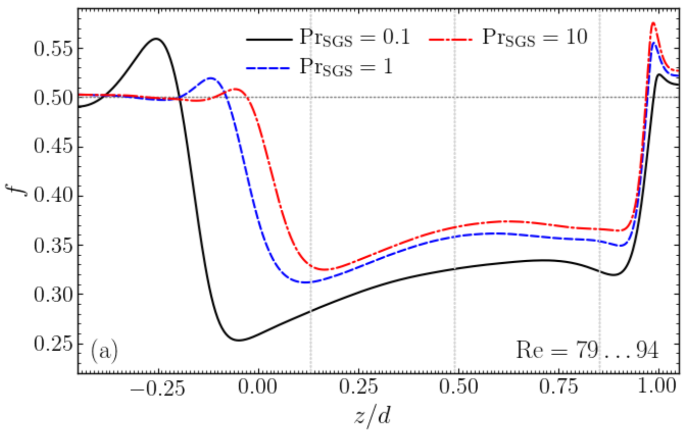

Figure 11: Filling factor of downflows f as a function of depth for representative values of $\mathrm{Pr_{SGS}}$ with $\mathrm{Re} \approx 79\ldots94$. Adapted from Paper VII.

3.3.2 Effects on the differential rotation in semi-global models (Paper IX)

In Paper IX the starting point is opposite to the premise in several recent studies where a high effective Prandtl number was assumed for the Sun (e.g. Bekki *et al.* 2017; Karak *et al.* 2018). There is no conclusive evidence of this (see, e.g. Käpylä & Singh 2022), and the microscopic Prandtl number in the solar and stellar convection zones is $\mathrm{Pr} \ll 1$. Furthermore, the results of Prandtl number sensitivity from earlier studies using Cartesian simulations (Paper III, Paper VII) suggest that the Prandtl number is likely to have an impact also for global properties of convection.

The main question studied in Paper IX is whether the Prandtl number plays a role in the transition from anti-solar to solar-like differential rotation in semi-global wedge simulations. These models were done with and without dynamo-generated magnetic fields to probe also the influence of magnetic fields on this transition. The main diagnostic used in this study is the mean differential rotation at the equator:

$$\langle \Delta\tilde{\Omega}_{\rm eq}\rangle = \frac{\int_{r_{\rm in}}^{R} r^2[\tilde{\overline{\Omega}}(r,\theta_{\rm eq}) - 1]dr}{\int_{r_{\rm in}}^{R} r^2 dr}, \tag{22}$$

where $\theta_{\rm eq} = \pi/2$, $\overline{\Omega} = \Omega_0 + \overline{u}_\phi/r\sin\theta$, and the tildes indicate normalization by the rotation rate of the frame of reference, Ω_0. Given that $\langle\Delta\tilde{\Omega}_{\rm eq}\rangle > 0$ the simulation is classified as a solar-like rotator. This is a rather simplistic criterion but it has the advantage that it is free from complications caused by, e.g., equatorial

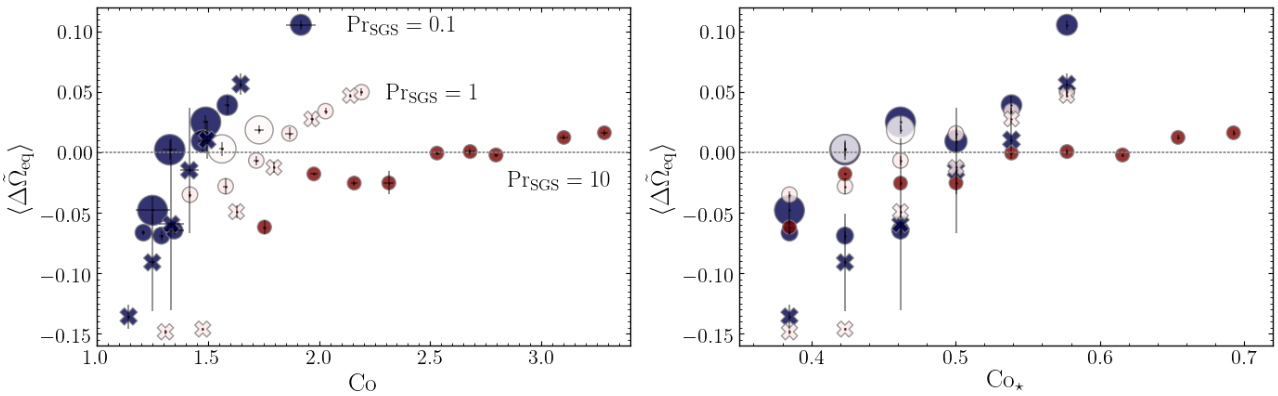

Figure 12: Measure of radial differential rotation $\langle \Delta\tilde{\Omega}_{\rm eq} \rangle$ at the equator of the star as a function of Co (left panel) and $\mathrm{Co}_\star$ (right panel). Crosses (circles) denote hydrodynamic (MHD) runs. The colours indicate the SGS Prandtl number as indicated in the left panel and the size of the symbol corresponds to Re ($\mathrm{Re_M}$) for hydrodynamic (MHD) cases. Adapted from Paper IX.

asymmetries in the rotation profile. A more sophisticated classification scheme including also the latitudinal differential rotation was introduced in Camisassa & Featherstone (2022).

Results from several sets of simulations from Paper IX with $\mathrm{Pr_{SGS}}$ varying between 0.1 and 10 are shown in Figure 12. The left panel shows that solar-like differential rotation is achieved at a lower Co for lower $\mathrm{Pr_{SGS}}$ as a general trend. Furthermore, the solar-like regime is reached at even lower Co in runs with dynamo-generated magnetic fields. A similar trend was seen with higher resolution simulations that are characterized by higher values of Re and $\mathrm{Re_M}$ and more turbulent flows and magnetic fields. The trend as a function of $\mathrm{Pr_{SGS}}$ agrees with the hydrodynamic simulations of Karak *et al.* (2018) who found that it is more difficult to obtain solar-like rotation profiles at high Prandtl numbers. However, Co as a measure of rotational influence relies on the convective velocity which is not known *a priori*. In Paper IX another form of the flux Coriolis number was used:

$$\mathrm{Co}_\star = \frac{2\Omega_0 R}{u_\star} = 2\Omega R^{5/3}\left(\frac{\rho}{L}\right)^{1/3} = (4\pi)^{-1/3}\left(\frac{R}{r_{\rm in}}\right)^2 \frac{R}{H}\,\mathrm{Co_F}, \tag{23}$$

where $r_{\rm in} = 0.7R$ is the radius of the base of the convection zone, and R is the radius of the star. In Paper IX, $\mathrm{Co}_\star = 0.5$ corresponds to a star with solar luminosity and rotation rate. When the results are recast in terms of $\mathrm{Co}_\star$, the trend as a function of the Prandtl number is weaker; see the right panel of Figure 12. While it is still clear that in the case with $\mathrm{Pr_{SGS}} = 10$ a solar-like differential rotation is more difficult to achieve, the differences between the $\mathrm{Pr_{SGS}} = 1$ and $\mathrm{Pr_{SGS}} = 0.1$ cases vanish. In this representation the roles of higher Reynolds numbers and magnetic fields are more pronounced. Small-scale magnetic fields have been suggested to be the primary cause for solar-like differential rotation with solar $\mathrm{Co_F}$ in high-resolution implicit Large-Eddy Simulations by Hotta & Kusano (2021) and Hotta *et al.* (2022). In the current cases a non-negligible effect of the magnetic field is observed, but the results do not change dramatically even when a small-scale dynamo is present. Therefore the effect of small-scale magnetic fields appears to be significantly weaker than in the simulations of Hotta *et al.* (2022).

Large-scale differential rotation in the Sun is thought to result in from turbulent angular momentum fluxes due to the convective motions. In mean-field hydrodynamics the angular momentum transport is represented by the turbulent Reynolds stress $Q_{ij} = \overline{\rho u_i' u_j'}$, where $\boldsymbol{u}' = \boldsymbol{u} - \overline{\boldsymbol{u}}$ is the velocity fluctuation and the overbar denotes suitable (now azimuthal) averaging (e.g. Rüdiger 1989; Kitchatinov & Rüdiger 1995; Kitchatinov & Rüdiger 2005). These theories adopt simple models for the turbulence to keep the analytics manageable and the detailed structure of flows producing such spectra is not addressed. On the other hand, rotating fluids support a rich variety waves, known as Rossby waves (e.g. Zaqarashvili *et al.* 2021; Gizon *et al.* 2021). One particular variant is the thermal Rossby wave which often manifests itself at the equatorial regions of rotating convecting spheres near the onset of convection (e.g. Hindman & Jain 2022). The Reynolds stresses and the resulting differential rotation from such waves was first studied by Busse in the early 1970s (Busse 1970b,a), and the columnar convective structures are therefore named Busse columns. Such convective modes are very prominent also in non-linear global numerical simulations (e.g. Miesch *et al.* 2008, see also Paper IV and the middle panel on Figure 3). In Paper IX the spatial scales of the Reynolds stress was studied using data in the

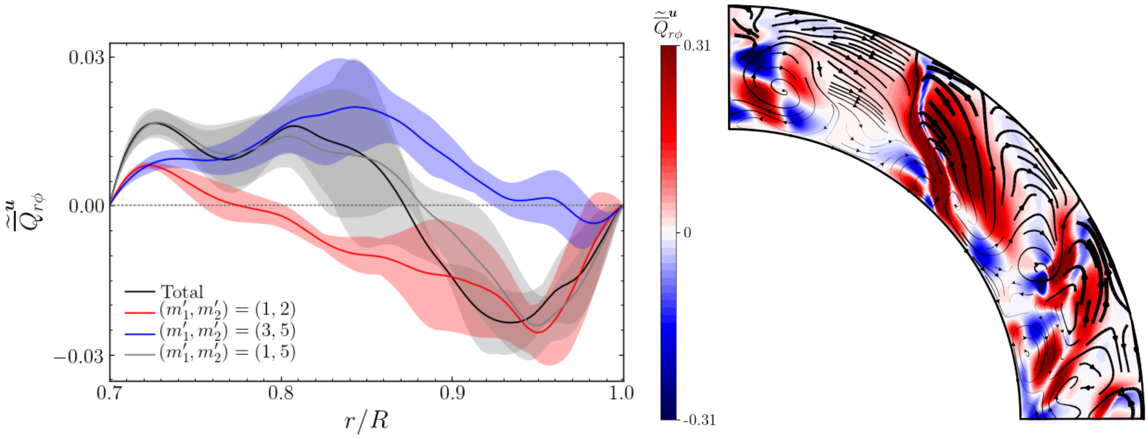

Figure 13: Left panel: Contributions from low-order azimuthal modes to the radial Reynolds stress $\tilde{\overline{Q}}^{u}_{r\phi}$ at the equator of the star. Right panel: Instantaneous velocity field (arrows) and radial angular momentum flux $\tilde{\overline{Q}}^{u}_{r\phi}$ (colour contours) from a simulation with solar-like differential rotation. Adapted from Paper IX.

equatorial plane of the star as a function of the azimuthal modes m'. A representative result is shown in the left panel of Figure 13. If only the two first modes $m' = 1, 2$ are retained the resulting radial Reynolds stress $\tilde{\overline{Q}}^{u}_{r\phi}$ ($\propto Q_{r\phi}$) is mostly negative. However, the $m' = 3 \ldots 5$ modes yield a positive $\tilde{\overline{Q}}^{u}_{r\phi}$, and the combined stress from modes $(m'_1, m'_2) = (1, 5)$ is almost the same as the total stress where in this particular case $m'_{\rm max} = 72$. The conclusion is that the positive $\tilde{\overline{Q}}^{u}_{r\phi}$ that is needed to drive solar-like differential rotation comes almost solely from relatively large-scale structures that can be identified as the Busse columns; see the right panel of Figure 13. In Paper IX this conclusion remains the same also in the cases where both large-scale and small-scale dynamos are excited. Similar large-scale structures are also visible in the high-resolution simulations of Hotta *et al.* (2022) even though in their simulations the effect of the magnetic field on the differential rotation was more pronounced. The dominance of such large-scale structures in simulations in comparison to them being apparently very weak in the Sun remains puzzling.

4 Solar and stellar dynamos

In astrophysics the main interest to simulate convection is connected to the generation of large-scale magnetic fields in stars and planets such at the Sun and the Earth. As discussed above, the details of stellar convection appear to be less well understood than previously thought. The changing paradigm of stellar convection has wider repercussions for dynamos in stars of different ages and masses such that the plausibility of different dynamo mechanisms need to be re-evaluated. The solar case is especially intriguing because the Sun appears to be near a transition from solar-like to anti-solar differential rotation which is likely to have major implications for its dynamo (e.g. van Saders *et al.* 2016; Metcalfe *et al.* 2016). It may well be that modeling the solar dynamo is particularly difficult because of its proximity to the differential rotation transition (Käpylä *et al.* 2023). Although this transition is typically not captured at the correct Coriolis number in simulations (e.g., Paper II), it is nevertheless still possible to study the rotational evolution of dynamo solutions in stars bearing this offset in mind. A similar argument applies to stars of different masses and depths of convection zones and to comparisons with observations. The topics covered here include rotational evolution of dynamos and dynamo cycles in solar-like stars (Paper II, Paper VIII), dynamos in fully convective stars (Paper VI), and the effects of subadiabatic layers on large-scale differential rotation and dynamos (Paper IV).

4.1 Dynamos in solar-type stars as a function of rotation (Paper II, Paper VIII)

An important question in the study stellar magnetism is the evolution of the dynamos as a function of time. While the other stellar parameters do not change appreciably during the main-sequence lifetime of late-type stars, the rotation of stars gradually slows down because of the coupling of the stellar magnetic fields with the surrounding interstellar medium (e.g Skumanich 1972; Barnes 2003). Abundant observational evidence indicates that stellar magnetism intensifies as a function of rotation and that for sufficiently rapid rotation the activity plateaus (e.g. Wright *et al.* 2011, 2018; Reiners *et al.* 2022). Rotation is a crucially important ingredient

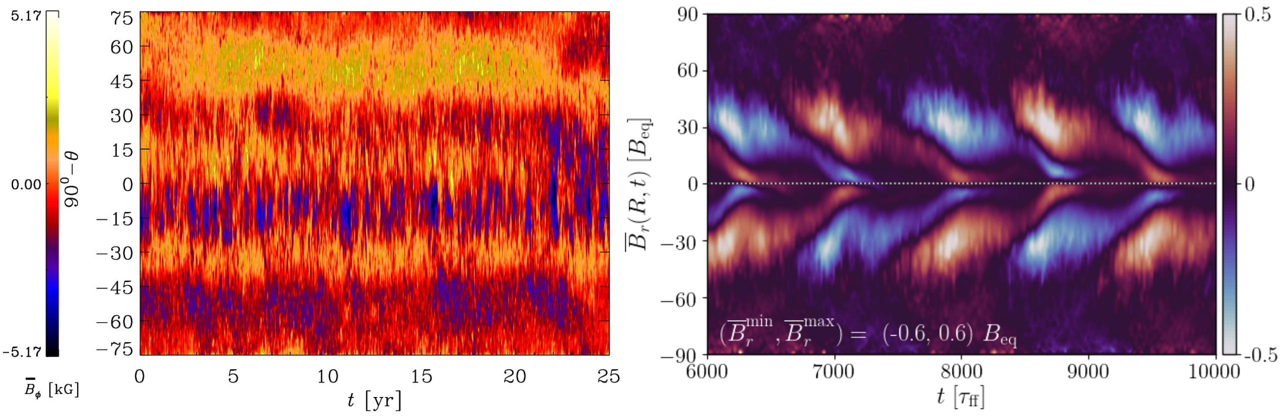

Figure 14: Left: Time-latitude diagram of the longitudinally averaged azimuthal field $\overline{B}_\phi$ from a simulation of a slowly rotating solar-like star with anti-solar differential rotation. Adapted from Käpylä *et al.* (2017). Right: Azimuthally averaged radial magnetic field $\overline{B}_r$ near the surface of the star in a star-in-a-box simulation of a solar-like star. Adapted from Paper VIII.

in stellar dynamos because it is related to both generation of differential rotation and magnetism via its effects on the statistics of turbulent flows driven by convection (e.g. Krause & Rädler 1980; Rüdiger 1989; Moffatt & Dormy 2019). Thus the study of convective dynamos as a function of rotation is necessary to develop a stellar dynamo theory. The solar dynamo must fit into this larger picture and therefore studies of the Sun should be done as a part of a more general effort adn not in isolation. Furthermore, observations of the field topologies and cycles of the Sun and other stars provide constraints to the theoretical models and simulations. The solar cyclic dynamo is the most well-documented case, but there are many other stars where cycles have been observed from long-term surveys of magnetically active spectral lines such as Ca II H&K (e.g. Baliunas *et al.* 1995; Saar & Brandenburg 1999; Olspert *et al.* 2018). Whereas the solar large-scale magnetic field is predominantly axisymmetric, mean-field models based on classical mean-field dynamo theory suggest that at sufficiently rapid rotation the large-scale magnetic fields become increasingly non-axisymmetric (e.g. Moss & Brandenburg 1995). Such magnetic field configurations have been reported from Zeeman-Doppler Imaging of rapidly rotating late-type stars (e.g. Kochukhov *et al.* 2013) and hints of a transition from predominantly axisymmetric to non-axisymmetric fields have been reported from photometric studies (e.g. Lehtinen *et al.* 2016).

While earlier studies had covered limited ranges of a few values in rotation rate (e.g. Brown *et al.* 2011; Käpylä *et al.* 2013, 2017), a comprehensive study was undertaken in Paper II, where spherical wedge simulations covering the full 2π longitude range were used, and where the Coriolis number was varied between 1.4 and 126, corresponding to physical rotation rates $\Omega_\odot \ldots 31\Omega_\odot$ ($P_{\rm rot} \approx 30 \ldots 1$ day). These simulations show that when rotation is slow enough such that anti-solar differential rotation develops, the resulting large-scale dynamos are predominantly axisymmetric and quasi-static; see a representative example from Käpylä *et al.* (2017) in the left panel of Figure 14; (see also, e.g. Strugarek *et al.* 2018; Warnecke 2018). At somewhat more rapid rotation, a solar-like differential rotation is achieved with a corresponding change in the dynamo mode. The large-scale fields continue to be predominantly axisymmetric but now they exhibit cycles. There is considerable debate whether observed stellar cycles show systematic trends – or activity branches – as a function of rotation; see discussions in Brandenburg *et al.* (2017), Olspert *et al.* (2018), Boro Saikia *et al.* (2018), and Irving *et al.* (2023) with different authors coming to contradicting conclusions using partially the same data but different

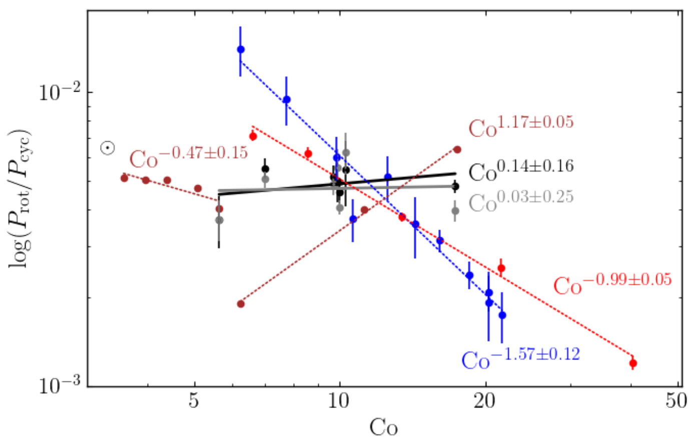

Figure 15: Ratio of the rotation period ($P_{\rm rot}$) to cycle period ($P_{\rm cyc}$) as a function of Co from simulations of stellar dynamos. Data from Paper VIII (b;ack and grey), Strugarek *et al.* (2018) (blue), Warnecke (2018) (red), and Guerrero *et al.* (2019) (brown) are shown. Adapted from Paper VIII.

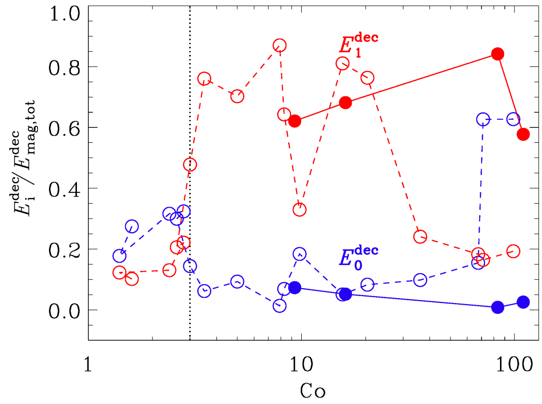

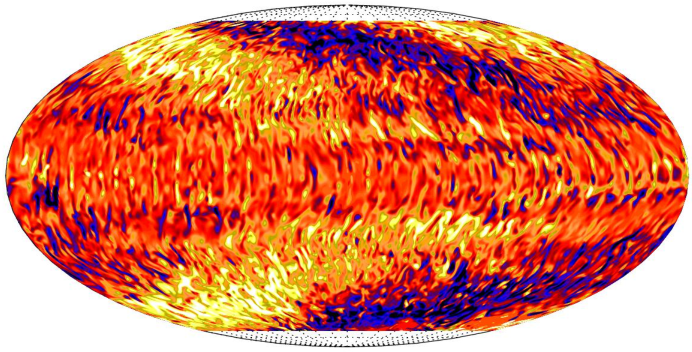

Figure 16: Left panel: relative energies of the axisymmetric ($m = 0$, blue circles), and the first non-axisymmetric ($m = 1$, red circles) modes as a function of Co. The filled circles denote results from high resolution runs. Right panel: Mollweide projection of the radial surface magnetic field B_r from a simulation of a solar-like star rotating at $\Omega_0 = 5\Omega_\odot$. Adapted from Paper II.

methods. A similarly complex situation is encountered with simulations results; see Figure 15 where a commonly used diagnostic $P_{\rm rot}/P_{\rm cyc}$ is shown as a function of Co from various numerical studies. The activity branches advocated by Brandenburg *et al.* (2017) have $P_{\rm rot}/P_{\rm cyc} \propto {\rm Co}^\beta$ where $\beta > 0$ whereas most numerical studies yield $\beta \approx -1$. The simulations in Paper VIII are currently the only ones where $\beta \approx 0$ or even somewhat positive systematically over a limited range of Co. The reasons for such heterogeneous behavior are as of yet unclear and require more concentrated efforts to distinguish the dominant dynamo effects, e.g., via detailed mean-field modelling (e.g. Warnecke *et al.* 2021).

In many of the early simulations the cycles showed poleward propagation in contradiction to the Sun (e.g. Gilman 1983; Glatzmaier 1985; Käpylä *et al.* 2010; Brown *et al.* 2011). As explained in Section 1, reproducing the solar equatorward migrating pattern of activity remains challenging for the current simulations. Nevertheless, such solutions have been obtained by many research groups and a wide variety of numerical approaches (e.g. Käpylä *et al.* 2012; Augustson *et al.* 2015; Duarte *et al.* 2016; Matilsky & Toomre 2020); see a recent example from star-in-a-box models from Paper VIII in the right panel of Figure 14. However, it is questionable whether any of these simulations captures the actual dynamo process in the Sun. As shown in Warnecke *et al.* (2014) and Warnecke *et al.* (2018), the equatorward propagation in most of these simulations is very likely caused by a feature in the differential rotation profile that does not appear in the Sun. Another aspect regarding cycles is that the dynamo solutions are sensitive to the boundary conditions used in the simulations; see Warnecke *et al.* (2016) and Paper VIII. In the latter study the star-in-a-box model was used and there is no explicit boundary condition at the surface of the star. However, by varying the magnetic diffusivity in the exterior of the star, the boundary condition is effectively changed. In particular, if the resistivity in the exterior is increased the cyclic solutions give way to a quasi-static mode. The greater freedom of the magnetic field near the stellar surface in the star-in-a-box simulations may also contribute to the qualitatively different behavior of the cycles in these simulations in comparison to other numerical studies; see Figure 15.

The results of Paper II suggest that the window in which cyclic solutions appear is rather narrow (see also Strugarek *et al.* 2018; Brun *et al.* 2022). Furthermore, the large-scale magnetic fields become increasingly dominated by low order non-axisymmetric modes for more rapid rotation. This is illustrated in the left panel of Figure 16 where the energy fraction contained in the axisymmetric ($m = 0$) and the first non-axisymmetric modes ($m = 1$) with respect to the total magnetic energy are shown. The transition to non-axisymmetrically dominated dynamos occurs around ${\rm Co} = 3$ which correspond to $\Omega \approx 1.8\Omega_\odot$. In these simulations this also coincides with the transition from anti-solar to solar-like differential rotation whereas observational studies (e.g. Lehtinen *et al.* 2016) put the transition to non-axisymmetric fields at more rapid rotation. This suggests that the simulations capture qualitatively correct behavior. At sufficiently rapid rotation the large-scale non-axisymmetric fields are strong enough so that they are immediately apparent in maps of the magnetic field; see the right panel of Figure 16. Another interesting feature is that these non-axisymmetric structures drift in longitude. Such azimuthal dynamo waves were reported from linear mean-field dynamo models already by Rädler (1980) and Krause & Rädler (1980), and they can be understood as analogues of the latitudinal dynamo waves such as those observed in the Sun. A hallmark of these waves is that they propagate like rigid

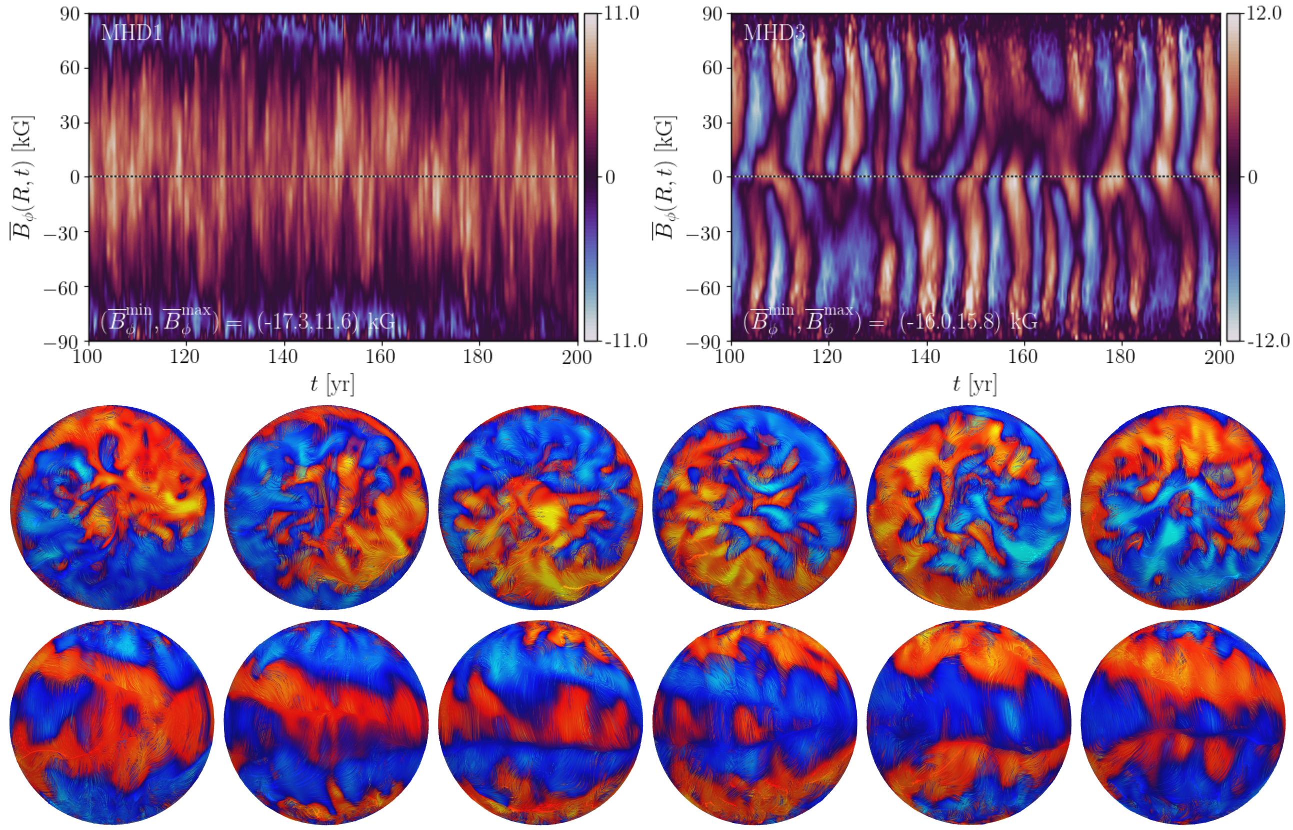

Figure 17: Top row: Time-latitude diagrams of the azimuthally averaged toroidal magnetic field $\overline{B}_\phi$ near the surface of a fully convective $0.2M_\odot$ star with slow ($P_{\rm rot} = 430$ days; left) and intermediate ($P_{\rm rot} = 43$ days; right) rotation rates. The two lower rows show the radial magnetic field near the surface of a rapidly rotating star with $P_{\rm rot} = 4.3$ days at six epochs facing the pole (middle row) and the equator (lower row). Adapted from Paper VI.

bodies independently of the fluid velocity (e.g. Cole *et al.* 2014; Viviani & Käpylä 2021; Navarrete *et al.* 2023, Paper II). There is also observational evidence that the rotation periods of magnetic features differ from those of the actual stellar rotation which can be interpreted as the presence of azimuthal dynamo waves (Lehtinen *et al.* 2016). Spot tracking is often used to measure differential rotation in stars other than the Sun. The existence of azimuthal dynamo waves, that can be prograde or retrograde (e.g. Navarrete *et al.* 2023), makes such methods potentially highly unreliable, even to the extent that the overall sense of the inferred differential rotation may be incorrect.

4.2 Dynamos in fully convective stars as a function of rotation (Paper VI)

The solar interior rotation profile Figure 1 shows relatively little radial shear within the convection zone while regions of strong radial shear are present in the boundary layers at the base and near the surface. The lower shear layer, which is known as the *tachocline*, plays a very prominent role in a class of solar dynamo models known as flux-transport dynamos (e.g. Dikpati & Charbonneau 1999). In this model the poloidal magnetic fields are amplified by the strong shear below the convection zone to strengths in excess of 100 kG before erupting to the surface (e.g. Schüssler *et al.* 1994). This is in contrast to the distributed turbulent dynamos where the magnetic fields are thought to be amplified throughout the convection zone due to the interaction of rotation and convection (e.g. Parker 1955; Steenbeck *et al.* 1966). On the other hand, late-type M stars with masses below about $0.35M_\odot$ are thought to be fully convective (e.g. Chabrier & Baraffe 1997) such that no tachocline can exist. Based on the flux transport dynamo paradigm, it has been postulated that dynamos in fully convective stars have to be driven by some completely different mechanism than in their partially convecting higher mass counterparts. Yet fully convective M dwarfs also exhibit vigorous global-scale magnetism (Kochukhov 2021) and X-ray emission that is in line with partially convective stars (e.g. Wright *et al.* 2018). Therefore fully convective stars are very important in the general picture of stellar magnetism and dynamos in that they can be used to narrow down the spectrum of plausible stellar dynamo scenarios.

Prior numerical works have concentrated on magnetic field generation in fully convective stars in isolated

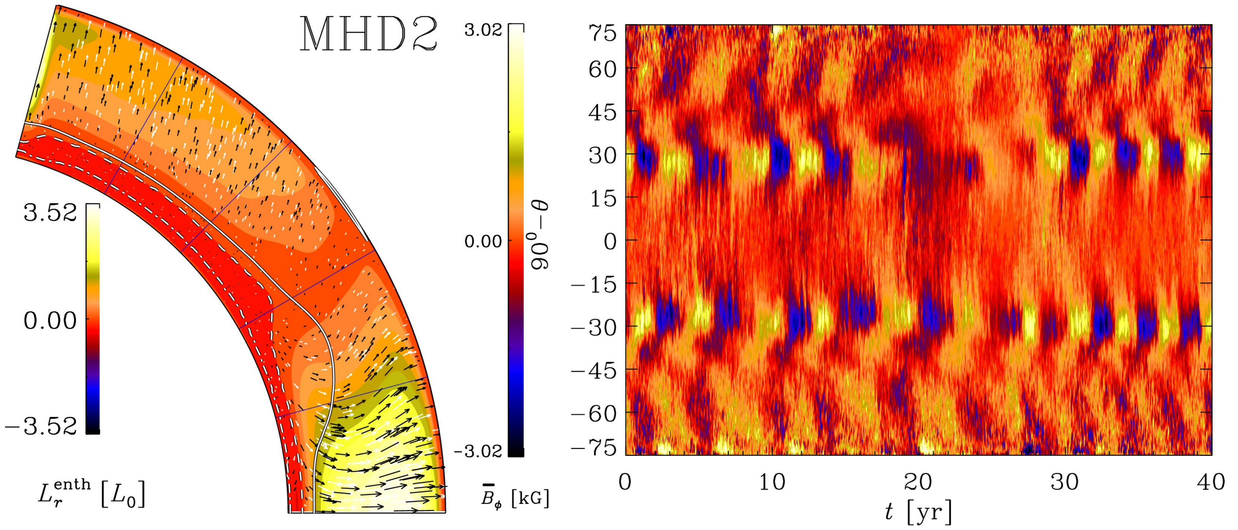

Figure 18: Left: Time-averaged radial component of the enthalpy flux $L_r^{\rm enth}$ (colour contours) and the vectorial enthalpy flux (arrows) in the meridional plane of a solar-like star with $\Omega = 3\Omega_\odot$. The solid, dashed, and dash-dotted lines indicate the bottoms of the buoyancy, Deardorff, and overshoot zones. Right: Time-latitude diagram of the mean azimuthal magnetic field $\overline{B}_\phi(t,\theta)$ from the same simulation. Adapted from Paper IV.

case studies without systematic efforts to probe the rotation dependence of dynamos (e.g. Dobler *et al.* 2006; Browning 2008; Yadav *et al.* 2015b; Brown *et al.* 2020). A systematic study of this kind was undertaken in Paper VI, targeting a $0.2M_\odot$ fully convective star with star-in-a-box models with the rotation period $P_{\rm rot}$ varying between 4.3 and 430 days. The results for the large-scale dynamos are summarized in Figure 17. The similarity to partially convective stars is striking: slowly rotating simulations show anti-solar differential rotation with predominantly axisymmetric quasi-static dynamos, while at somewhat faster rotation solar-like rotation profile and cyclic solutions appear. Increasing the rotation rate further leads to non-axisymmetric fields that exhibit azimuthal dynamo waves. Taken at face value, the results of Paper VI suggest that dynamos in fully convective stars are driven by the same process as in more massive partially convecting stars. This conjecture comes with the caveat that it is yet to be clarified whether the simulations in either case capture the correct stellar dynamo processes.

The current spherical wedge and star-in-a-box simulations have not yielded any dipole-dominated dynamos in the rapid rotation regime, unlike some other numerical studies (e.g. Yadav *et al.* 2015a; Zaire *et al.* 2022). It is unclear why such solutions do not appear, but a possibility is that the missing polar caps in spherical wedges and/or the additional conducting exterior in the star-in-a-box simulations is the cause. The dependence of dynamo solutions to boundary conditions has already been mentioned earlier and this is another possibility. Therefore more effort in the future needs to be made to set up benchmarks that probe the effects of different geometries, boundary conditions, and other modelling choices.

4.3 Effects of subadiabatic layers on global dynamos (Paper IV)

The results discussed in Section 3.1 imply that the canonical convection modelling paradigm has to be revised to take into account the convecting yet stably stratified Deardorff layers in deep convection zones. An extended stably stratified layer at the base of the convection zone has important implications for global dynamos. For instance, magnetic fields are less susceptible to rise buoyantly in stably stratified layers, thus allowing stronger fields to reside within the convection zone. Furthermore, deep overshooting or Deardorff layers can also lead to an extended helicity inversion layer that has been shown to result in solar-like equatorward migrating dynamo wave Duarte *et al.* (2016). The most straightforward way in which a Deardorff layer can be realized is to allow a smoothly varying heat conductivity connecting the radiative and convective regions (Paper I). Therefore the Kramers opacity law was implemented in semi-global wedge simulations that are used to model convection and dynamos of solar-like stars in Paper IV.

A representative result of the enthalpy luminosity, $L_r^{\rm enth} = 4\pi r^2 F_r^{\rm enth}$, and the interior structure in terms of buoyancy, Deardorff and overshoot layers is shown in the left panel of Figure 18. The enthalpy flux is highly anisotropic with maxima at the equator and at the highest latitudes retained in the model. With the exception of the equatorial regions, the enthalpy flux has a systematic poleward component. The absolute magnitude of the latitudinal anisotropy is much larger than that expected in real stars because we used ELM; see Section 2.3. To obtain an estimate for the latitude variation with realistic luminosity, the relevant scaling relations need to be applied (Paper III,Paper V). The enthalpy luminosity scales proportional to $L_{\rm ratio}$ which in this case is $2.1 \cdot 10^5$, meaning that the latitudinal flux variation in a real star is smaller by this factor. Furthermore, if a fixed profile of K is used, the anisotropy is even larger than in the case where the Kramers opacity laws; see Paper V. Nevertheless, recent helioseismic results suggest that deep convection in the Sun is indeed more vigorous near the equator Hanasoge *et al.* (2020).

The anisotropy of the enthalpy flux is also imprinted in the latitudinal variation of the depths of the Deardorff and overshoot layers. Figure 18 shows that the Deardorff layer is in general very shallow except at midlatitudes. This can be understood in light of the results obtained in Paper X: convection in these simulations is already sufficiently constrained by rotation such that the Deardorff layer is reduced due to the decreasing anisotropy between upflows and downflows. Furthermore, the simulations in Paper IV have $\mathrm{Pr}_{\rm eff} = 1$ which may not be representative of convection occurring in real stars; see the discussion Section 3.3 and Paper VII.

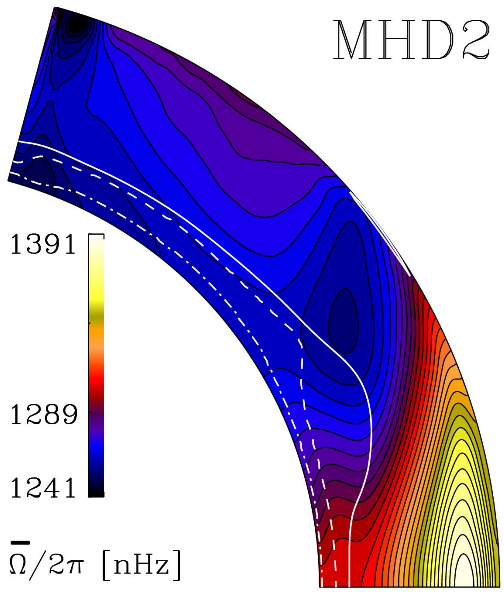

Figure 19: Internal rotation profile of the same simulation as in Figure 18. Adapted from Paper IV.

Given that the Deardorff layers in the rotating semi-global simulations are quite shallow it is therefore not a major surprise that the dynamo solutions are not very different from models where Deardorff layers are absent; see the right panel of Figure 18. This is very similar to several earlier simulations with a fixed profile of heat conductivity (e.g. Käpylä *et al.* 2012; Warnecke *et al.* 2014; Warnecke 2018). Such solar-like solutions are obtained on a limited range of parameters and the equatorward migration is explained be a mid-latitude minimum of $\overline{\Omega}$; (Warnecke *et al.* 2014, 2018, see also Figure 19). This feature is absent from the helioseismically obtained rotation profile of the Sun; see Figure 1. The mid-latitude minimum of $\overline{\Omega}$ in simulations can be explained by the large-scale Busse columns near the equator that appear inside the tangent cylinder. The absence of this feature in the Sun is another hint that essential features of deep solar convection are not yet captured by the current simulations.

5 Conclusions and future directions

The observational and numerical results during the last decade or so indicate fairly clearly that the current understanding of stellar convection is incomplete. Nevertheless, numerical simulations are an invaluable tool to study fundamental dynamo mechanisms in various kinds of stars. My research has touched several aspects of these issues and the key topics of the publications included in this dissertation can be categorized in three groups:

1. Studies of fully compressible model setups that use the enhanced luminosity method (ELM) and clarify scalings relations between simulations and stars with realistic luminosity (Paper V). Furthermore, the scaling of various dynamical quantities such as convective overshooting (Paper III), velocity (Paper III, Paper X), and temperature fluctuations (Paper V) as functions of the luminosity excess were confirmed numerically. The ELM models enable running simulations to thermal relaxation (Paper IX) which is typically infeasible with realistic luminosities. The most significant result from these studies is that the convective overshooting is less strongly dependent on the luminosity that previously thought and that in a simulation with luminosity excess of 10^6 the overshooting may only be three times deeper than with the realistic luminosity.

2. Targeted studies of deep stellar convection probing the effects of subadiabatic layers (Paper I, Paper III), rotation (Paper X), Prandtl number in local (Paper VII) and semi-global models (Paper IX). These studies showed that the deep parts of convection zones are likely to have subadiabatic layers if the convective

and radiative layers connect smoothly (Paper I, Paper III). The results of Paper X show that while hydrodynamic convection follows the CIA scaling, the flows in deep solar convection zone are not strongly rotationally constrained and that the effect of rotation is unable to reduce the dominant scale of convection sufficiently to account for the convective conundrum. All of these simulations were made with a thermal Prandtl number near unity whereas in stellar convection zones $\mathrm{Pr} \ll 1$. The asymmetry between upflows and downflows and the corresponding energy transport efficiency was shown to be sensitive to the Prandtl number in Paper VII. These effects were particularly pronounced when the Prandtl number was smaller than unity, implying that convection in stars can indeed be quite different to what current simulations lead us to believe. However, in Paper IX the transition of differential rotation from anti-solar to solar-like state was shown to be more sensitive to magnetic fields than to the Prandtl number.

3. Studies of global dynamos as functions of stellar age (Paper II, Paper VIII) and mass (Paper VI), and the effects of subadiabatic layers of dynamos (Paper IV). The most striking result here is the similar evolution of large-scale dynamos as a function of rotation in solar-like stars with a convective envelope (Paper II) and in fully convective stars (Paper VI), suggesting that a universal mechanism is responsible for both. In accordance with previous studies, the range of parameters where the large-scale dynamo is predominantly axisymmetric and cyclic is rather narrow (Paper II, Paper VIII), and that the behavior of the cycles as a function of rotation is sensitive to yet undiscovered details of the models (Paper VIII). The effect of a subadiabatic layer on the dynamo solutions was shown to be weak in Paper IV, but this is subject to the caveat that such layers can be significantly deeper in real stars.

While there has been significant progress in the understanding of stellar convection over the past years, with some contributions described in the present thesis, several open questions remain. The most prominent of these is the apparent absence of large-scale velocity power, especially the thermal Rossby waves and giant cells, in the Sun as opposed to simulations. Another major issue is that the solar dynamo remains mysterious in the sense that no 3D simulation captures it accurately. Furthermore, the transitions of differential rotation and dynamo modes in stars other than the Sun occur at different rotation rates than in simulations. In the opinion of the current author, the cause of all of these questions lies very likely in the inability of the current simulations to capture the true essence of deep stellar convection with sufficient fidelity. Therefore further development of models that can reach more realistic flows and magnetic fields, and that can more accurately capture the surface-driven small scale entropy rain are required. In light of the prohibitive numerical constraints, major advancements are less likely to come from brute force efforts than from clever ways to incorporate the unresolved small scales in global models. These are likely to employ modelers for many years to come.

Bibliography

Arlt, R. & Vaquero, J.M. (2020). *Living Reviews in Solar Physics*, **17**, 1

Augustson, K., Brun, A.S., Miesch, M., & Toomre, J. (2015). *ApJ*, **809**, 149

Augustson, K.C., Brun, A.S., & Toomre, J. (2013). *ApJ*, **777**, 153

Augustson, K.C., Brun, A.S., & Toomre, J. (2016). *ApJ*, **829**, 92

Augustson, K.C., Brun, A.S., & Toomre, J. (2019). *ApJ*, **876**, 83

Aurnou, J.M., Horn, S., & Julien, K. (2020). *Physical Review Research*, **2**, 043115

Baliunas, S.L. *et al.* (1995). *ApJ*, **438**, 269

Ballot, J., Brun, A.S., & Turck-Chièze, S. (2007). *ApJ*, **669**, 1190

Barker, A.J., Dempsey, A.M., & Lithwick, Y. (2014). *ApJ*, **791**, 13

Barnes, S.A. (2003). *ApJ*, **586**, 464

Bekki, Y., Hotta, H., & Yokoyama, T. (2017). *ApJ*, **851**, 74

Böhm-Vitense, E. (1958). *ZAp*, **46**, 108

Boro Saikia, S. *et al.* (2018). *A&A*, **616**, A108

Brandenburg, A. (2016). *ApJ*, **832**, 6

Brandenburg, A., Mathur, S., & Metcalfe, T.S. (2017). *ApJ*, **845**, 79

Brandenburg, A., Nordlund, Å., & Stein, R.F. (2000). *Astrophysical Convection and Dynamos*, pp. 85–105 (Gordon and Breach Science Publishers)

Breuer, M., Wessling, S., Schmalzl, J., & Hansen, U. (2004). *Phys. Rev. E*, **69**, 026302

Brown, B.P., Miesch, M.S., Browning, M.K., Brun, A.S., & Toomre, J. (2011). *ApJ*, **731**, 69

Brown, B.P., Oishi, J.S., Vasil, G.M., Lecoanet, D., & Burns, K.J. (2020). *ApJ*, **902**, L3

Browning, M.K. (2008). *ApJ*, **676**, 1262

Brun, A.S., Miesch, M.S., & Toomre, J. (2004). *ApJ*, **614**, 1073

Brun, A.S. *et al.* (2022). *ApJ*, **926**, 21

Busse, F.H. (1970a). *ApJ*, **159**, 629

Busse, F.H. (1970b). *Journal of Fluid Mechanics*, **44**, 441

Camisassa, M.E. & Featherstone, N.A. (2022). *ApJ*, **938**, 65

Carrington, R.C. (1863). *Observations of the Spots on the Sun* (London)

Cattaneo, F., Brummell, N.H., Toomre, J., Malagoli, A., & Hurlburt, N.E. (1991). *ApJ*, **370**, 282

Chabrier, G. & Baraffe, I. (1997). *A&A*, **327**, 1039

Chandrasekhar, S. (1961). *Hydrodynamic and hydromagnetic stability*

Charbonneau, P. (2020). *Living Reviews in Solar Physics*, **17**, 4

Christensen, U.R. (2002). *Journal of Fluid Mechanics*, **470**, 115

Christensen, U.R. & Aubert, J. (2006). *Geophys. J. Int.*, **166**, 97

Cole, E., Käpylä, P.J., Mantere, M.J., & Brandenburg, A. (2014). *ApJL*, **780**, L22

Deardorff, J.W. (1961). *J. Atmosph. Sci.*, **18**, 540

Deardorff, J.W. (1966). *J. Atmosph. Sci.*, **23**, 503

Dikpati, M. & Charbonneau, P. (1999). *ApJ*, **518**, 508

Dobler, W., Stix, M., & Brandenburg, A. (2006). *ApJ*, **638**, 336

Duarte, L.D.V., Wicht, J., Browning, M.K., & Gastine, T. (2016). *MNRAS*, **456**, 1708

Edwards, J.M. (1990). *MNRAS*, **242**, 224

Featherstone, N.A. & Hindman, B.W. (2016). *ApJ*, **830**, L15

Ghizaru, M., Charbonneau, P., & Smolarkiewicz, P.K. (2010). *ApJ*, **715**, L133

Gilman, P.A. (1977). *Geophys. Astrophys. Fluid Dynam.*, **8**, 93

Gilman, P.A. (1983). *ApJS*, **53**, 243

Gilman, P.A. & Miller, J. (1981). *ApJS*, **46**, 211

Gizon, L. *et al.* (2021). *A&A*, **652**, L6

Glatzmaier, G.A. (1984). *Journal of Computational Physics*, **55**, 461

Glatzmaier, G.A. (1985). *ApJ*, **291**, 300

Greer, B.J., Hindman, B.W., Featherstone, N.A., & Toomre, J. (2015). *ApJ*, **803**, L17

Guerrero, G., Stejko, A.M., Kosovichev, A.G., Smolarkiewicz, P.K., & Strugarek, A. (2022). *ApJ*, **940**, 151

Guerrero, G. *et al.* (2019). *ApJ*, **880**, 6

Hale, G.E. (1908). *ApJ*, **28**, 315

Hale, G.E., Ellerman, F., Nicholson, S.B., & Joy, A.H. (1919). *ApJ*, **49**, 153

Hanasoge, S.M., Duvall, T.L., & Sreenivasan, K.R. (2012). *Proc. Natl. Acad. Sci.*, **109**, 11928

Hanasoge, S.M., Hotta, H., & Sreenivasan, K.R. (2020). *Science Advances*, **6**, eaba9639
Hindman, B.W. & Jain, R. (2022). *ApJ*, **932**, 68
Hotta, H. (2017). *ApJ*, **843**, 52
Hotta, H. & Kusano, K. (2021). *Nature Astronomy*, **5**, 1100
Hotta, H., Kusano, K., & Shimada, R. (2022). *ApJ*, **933**, 199
Irving, Z.A., Saar, S.H., Wargelin, B.J., & do Nascimento, J.D. (2023). *ApJ*, **949**, 51
Jermyn, A.S., Anders, E.H., Lecoanet, D., & Cantiello, M. (2022). *ApJS*, **262**, 19
Käpylä, P.J., Browning, M.K., Brun, A.S., Guerrero, G., & Warnecke, J. (2023). *Space Sci. Rev.*, **219**, 58
Käpylä, P.J., Käpylä, M.J., & Brandenburg, A. (2014). *A&A*, **570**, A43
Käpylä, P.J., Käpylä, M.J., Olspert, N., Warnecke, J., & Brandenburg, A. (2017). *A&A*, **599**, A4
Käpylä, P.J., Korpi, M.J., Brandenburg, A., Mitra, D., & Tavakol, R. (2010). *Astron. Nachr.*, **331**, 73
Käpylä, P.J., Korpi, M.J., Stix, M., & Tuominen, I. (2005). *A&A*, **438**, 403
Käpylä, P.J., Mantere, M.J., & Brandenburg, A. (2012). *ApJ*, **755**, L22
Käpylä, P.J., Mantere, M.J., Cole, E., Warnecke, J., & Brandenburg, A. (2013). *ApJ*, **778**, 41
Käpylä, P.J. & Singh, N.K. (2022). *Journal of Fluid Mechanics*, **952**, R1
Karak, B.B., Miesch, M., & Bekki, Y. (2018). *Physics of Fluids*, **30**, 046602
Kitchatinov, L.L. & Rüdiger, G. (1995). *A&A*, **299**, 446
Kitchatinov, L.L. & Rüdiger, G. (2005). *Astron. Nachr.*, **326**, 379
Kochukhov, O. (2021). *A&A Rev.*, **29**, 1
Kochukhov, O., Mantere, M.J., Hackman, T., & Ilyin, I. (2013). *A&A*, **550**, A84
Krause, F. & Rädler, K.H. (1980). *Mean-field Magnetohydrodynamics and Dynamo Theory* (Pergamon Press, Oxford)
Kupka, F. & Muthsam, H.J. (2017). *Liv. Rev. Comp. Astrophys.*, **3**, 1
Lantz, S.R. & Fan, Y. (1999). *ApJS*, **121**, 247
Lehtinen, J., Jetsu, L., Hackman, T., Kajatkari, P., & Henry, G.W. (2016). *A&A*, **588**, A38
Matilsky, L.I. & Toomre, J. (2020). *ApJ*, **892**, 106
Maunder, E.W. (1894). *Knowledge: An Illustrated Magazine of Science*, **17**, 173
Metcalfe, T.S., Egeland, R., & van Saders, J. (2016). *ApJ*, **826**, L2
Miesch, M.S., Brun, A.S., DeRosa, M.L., & Toomre, J. (2008). *ApJ*, **673**, 557
Moffatt, K. & Dormy, E. (2019). *Self-Exciting Fluid Dynamos*. Cambridge Texts in Applied Mathematics (Cambridge University Press)
Moss, D. & Brandenburg, A. (1995). *Geophys. Astrophys. Fluid Dyn.*, **80**, 229
Navarrete, F.H., Käpylä, P.J., Schleicher, D.R.G., & Banerjee, R. (2023). *A&A*, **678**, A9
Olspert, N., Lehtinen, J.J., Käpylä, M.J., Pelt, J., & Grigorievskiy, A. (2018). *A&A*, **619**, A6
O'Mara, B., Miesch, M.S., Featherstone, N.A., & Augustson, K.C. (2016). *Adv. Space Res.*, **58**, 1475
Orvedahl, R.J., Calkins, M.A., Featherstone, N.A., & Hindman, B.W. (2018). *ApJ*, **856**, 13
Ossendrijver, M. (2003). *A&A Rev.*, **11**, 287
Pandey, A., Schumacher, J., & Sreenivasan, K.R. (2021). *Physical Review Fluids*, **6**, 100503
Parker, E.N. (1955). *ApJ*, **122**, 293
Passos, D. & Charbonneau, P. (2014). *A&A*, **568**, A113
Pencil Code Collaboration *et al.* (2021). *The Journal of Open Source Software*, **6**, 2807
Proxauf, B. (2021). *Observations of large-scale solar flows*. Ph.D. thesis, Georg August University of Göttingen, Germany
Rädler, K.H. (1980). *Astronomische Nachrichten*, **301**, 101
Reiners, A. *et al.* (2022). *A&A*, **662**, A41
Rempel, M. (2004). *ApJ*, **607**, 1046
Roberts, P.H. (1968). *Philosophical Transactions of the Royal Society of London Series A*, **263**, 93
Rüdiger, G. (1989). *Differential Rotation and Stellar Convection. Sun and Solar-type Stars* (Akademie Verlag, Berlin)
Saar, S.H. & Brandenburg, A. (1999). *ApJ*, **524**, 295
Schou, J. *et al.* (1998). *ApJ*, **505**, 390
Schumacher, J. & Sreenivasan, K.R. (2020). *Reviews of Modern Physics*, **92**, 041001
Schüssler, M., Caligari, P., Ferriz-Mas, A., & Moreno-Insertis, F. (1994). *A&A*, **281**, L69
Schwabe, H. (1844). *Astronomische Nachrichten*, **21**, 233
Singh, H.P., Roxburgh, I.W., & Chan, K.L. (1998). *A&A*, **340**, 178
Skumanich, A. (1972). *ApJ*, **171**, 565

Speziale, C.G. (1991). *Annual Review of Fluid Mechanics*, **23**, 107
Spiegel, E.A. (1962). *J. Geophys. Res.*, **67**, 3063
Spruit, H. (1997). *Mem. Soc. Astron. Italiana*, **68**, 397
Steenbeck, M., Krause, F., & Rädler, K.H. (1966). *Zeitschrift Naturforschung Teil A*, **21**, 369
Stein, R.F. & Nordlund, A. (1989). *ApJ*, **342**, L95
Stein, R.F. & Nordlund, Å. (1998). *ApJ*, **499**, 914
Stevenson, D.J. (1979). *Geophysical and Astrophysical Fluid Dynamics*, **12**, 139
Strugarek, A., Beaudoin, P., Charbonneau, P., & Brun, A.S. (2018). *ApJ*, **863**, 35
Tian, C.L., Deng, L.C., & Chan, K.L. (2009). *MNRAS*, **398**, 1011
Tremblay, P.E. *et al.* (2015). *ApJ*, **799**, 142
Usoskin, I.G. (2023). *Living Reviews in Solar Physics*, **20**, 2
van Saders, J.L. *et al.* (2016). *Nature*, **529**, 181
Vasil, G.M., Julien, K., & Featherstone, N.A. (2021). *Proceedings of the National Academy of Science*, **118**, e2022518118
Vitense, E. (1953). *ZAp*, **32**, 135
Viviani, M. & Käpylä, M.J. (2021). *A&A*, **645**, A141
Viviani, M. *et al.* (2018). *A&A*, **616**, A160
Warnecke, J. (2018). *A&A*, **616**, A72
Warnecke, J., Käpylä, P.J., Käpylä, M.J., & Brandenburg, A. (2014). *ApJ*, **796**, L12
Warnecke, J., Käpylä, P.J., Käpylä, M.J., & Brandenburg, A. (2016). *A&A*, **596**, A115
Warnecke, J. *et al.* (2018). *A&A*, **609**, A51
Warnecke, J. *et al.* (2021). *ApJ*, **919**, L13
Weiss, A., Hillebrandt, W., Thomas, H.C., & Ritter, H. (2004). *Cox and Giuli's Principles of Stellar Structure* (Cambridge Scientific Publishers Ltd, Cambridge, UK)
Wright, N.J., Drake, J.J., Mamajek, E.E., & Henry, G.W. (2011). *ApJ*, **743**, 48
Wright, N.J., Newton, E.R., Williams, P.K.G., Drake, J.J., & Yadav, R.K. (2018). *MNRAS*, **479**, 2351
Yadav, R.K., Gastine, T., Christensen, U.R., & Reiners, A. (2015a). *A&A*, **573**, A68
Yadav, R.K. *et al.* (2015b). *ApJ*, **813**, L31
Zaire, B. *et al.* (2022). *MNRAS*, **517**, 3392
Zaqarashvili, T.V. *et al.* (2021). *Space Sci. Rev.*, **217**, 15